



**HAL**  
open science

## Convection and Differential Rotation in F-Type Stars

K.C. Augustson, Benjamin P. Brown, A.S. Brun, Mark S. Miesch, Juri Toomre

► **To cite this version:**

K.C. Augustson, Benjamin P. Brown, A.S. Brun, Mark S. Miesch, Juri Toomre. Convection and Differential Rotation in F-Type Stars. *The Astrophysical Journal*, 2013, 756 (2), pp.169. 10.1088/0004-637X/756/2/169 . cea-00827752

**HAL Id: cea-00827752**

**<https://cea.hal.science/cea-00827752>**

Submitted on 22 Jul 2020

**HAL** is a multi-disciplinary open access archive for the deposit and dissemination of scientific research documents, whether they are published or not. The documents may come from teaching and research institutions in France or abroad, or from public or private research centers.

L'archive ouverte pluridisciplinaire **HAL**, est destinée au dépôt et à la diffusion de documents scientifiques de niveau recherche, publiés ou non, émanant des établissements d'enseignement et de recherche français ou étrangers, des laboratoires publics ou privés.

## CONVECTION AND DIFFERENTIAL ROTATION IN F-TYPE STARS

KYLE C. AUGUSTSON<sup>1</sup>, BENJAMIN P. BROWN<sup>2</sup>, ALLAN SACHA BRUN<sup>3</sup>, MARK S. MIESCH<sup>4</sup>, AND JURI TOOMRE<sup>1</sup>

<sup>1</sup> JILA and Department of Astrophysical & Planetary Sciences, University of Colorado, Boulder, CO 80309, USA; [Kyle.Augustson@colorado.edu](mailto:Kyle.Augustson@colorado.edu)

<sup>2</sup> Department of Astronomy and Center for Magnetic Self-Organization (CMSO) in Laboratory and Astrophysical Plasmas, University of Wisconsin, Madison, WI 53706-1582, USA

<sup>3</sup> DSM/IRFU/SAP, CEA-Saclay and UMR AIM, CEA-CNRS-Université Paris 7, F-91191 Gif-sur-Yvette, France

<sup>4</sup> High Altitude Observatory, Center Green 1, Boulder, CO 80301, USA

Received 2012 March 24; accepted 2012 July 16; published 2012 August 24

### ABSTRACT

Differential rotation is a common feature of main-sequence spectral F-type stars. In seeking to make contact with observations and to provide a self-consistent picture of how differential rotation is achieved in the interiors of these stars, we use the three-dimensional anelastic spherical harmonic (ASH) code to simulate global-scale turbulent flows in 1.2 and 1.3  $M_{\odot}$  F-type stars at varying rotation rates. The simulations are carried out in spherical shells that encompass most of the convection zone and a portion of the stably stratified radiative zone below it, allowing us to explore the effects of overshooting convection. We examine the scaling of the mean flows and thermal state with rotation rate and mass and link these scalings to fundamental parameters of the simulations. Indeed, we find that the differential rotation becomes much stronger with more rapid rotation and larger mass, scaling as  $\Delta\Omega \propto M^{3.9}\Omega_0^{0.6}$ . Accompanying the growing differential rotation is a significant latitudinal temperature contrast, with amplitudes of 1000 K or higher in the most rapidly rotating cases. This contrast in turn scales with mass and rotation rate as  $\Delta T \propto M^{6.4}\Omega_0^{1.6}$ . On the other hand, the meridional circulations become much weaker with more rapid rotation and with higher mass, with their kinetic energy decreasing as  $KE_{MC} \propto M^{-1.2}\Omega_0^{-0.8}$ . Additionally, three of our simulations exhibit a global-scale shear instability within their stable regions that persists for the duration of the simulations. The flow structures associated with the instabilities have a direct coupling to and impact on the flows within the convection zone.

*Key words:* convection – hydrodynamics – stars: interiors – stars: rotation – stars: solar-type

*Online-only material:* color figures

## 1. INTRODUCTION

### 1.1. Stellar Convection and Rotation

Star-forming molecular clouds are generally endowed with angular momentum and magnetic fields. As a star forms, gases from the cloud fall into a proto-stellar region. Since the initial position of this gas is far from the stellar core, the initial angular velocity of the gas is amplified many orders of magnitude before it is incorporated into the star. The fact that most young stars are observed to have large rotation rates implies that, regardless of the complicated processes that initiate and eventually lead to the formation of a main-sequence star, some of this angular momentum must be transferred to the star. During the early evolution of these stars, it is thought that they lose their initially high angular velocity. Stellar winds and magnetic braking acting throughout the lifetime of the star may lead to such angular momentum loss (Bouvier et al. 1997). However, even after several billion years of angular momentum loss, stars such as the Sun still possess a substantial angular velocity. Indeed, stars with convective envelopes exterior to their radiative envelopes are believed to behave in qualitatively similar ways, where the complex interaction between the convection and the star's rotation likely yields non-uniform rotation. Hence, most stars may be differentially rotating, with the angular velocity varying with depth and latitude. The Sun is one such star, where the equator rotates 30% faster than the poles.

Main-sequence stars of all masses appear to have convection zones in some portions of their interiors. What makes F-type stars of particular interest is that they bridge a gap between stars that have external convection zones, like the Sun, and those

that have convective cores, such as A-type stars. They actually possess two regions of convective instability, one exterior to their radiative envelope and a convective core. Being slightly more massive than the Sun, F-type stars span the mass range between 1.1 and 1.6  $M_{\odot}$ . With increasing mass, the convection zones of these stars become increasingly narrow and contain less of the star's total mass, ranging from 25% to 2% of the radius of the star compared to the Sun's 30%. The luminosity of the F-type stars increases from about 1.4  $L_{\odot}$  at 1.1  $M_{\odot}$  to 6.0  $L_{\odot}$  at 1.6  $M_{\odot}$ , while the stellar radius only increases by about 27% over the same range of masses. Thus, the amount of energy flux that must be transported through ever thinner convection zones increases by a factor of 2.4. To accommodate the increasing flux, the convection must become more vigorous in order to efficiently transport the heat from the bottom of the convection zone to the photosphere. Such properties place F-type stars in an interesting position to address questions of how convection interacts with rotation and convection-zone geometry to produce differential rotation.

### 1.2. Observations of Differential Rotation

Detecting differential rotation in stars is very difficult as stars other than the Sun generally cannot be spatially resolved. However, recent observations using spectropolarimetry permit some information about both the differential rotation and the magnetic field to be mapped out on the surface of the star (e.g., Donati et al. 1997; Marsden et al. 2005). Several additional techniques exist to extract information about the rotational behavior of a star from spectra (e.g., Reiners & Schmitt 2003; Reiners 2006), photometry (e.g., Henry et al. 1995;

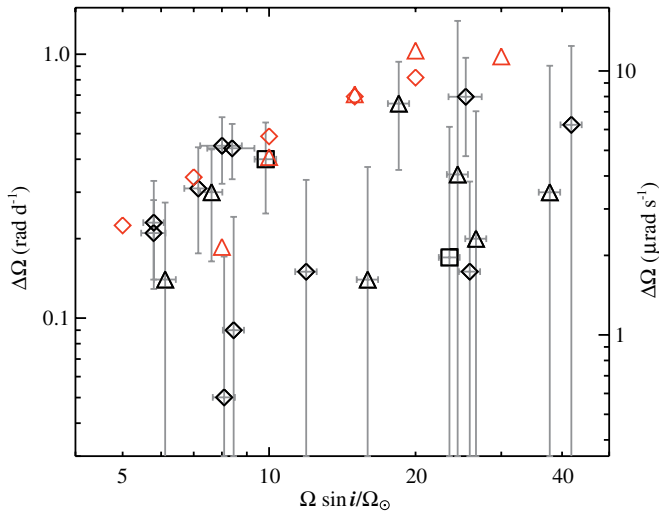


**Figure 1.** Absolute latitudinal differential rotation contrast ( $\Delta\Omega$ ) seen in simulations and observed on F-type stars. The observational uncertainties of the contrast and rotation rate are shown as gray lines. The values of the  $\Delta\Omega$  realized in our simulations are shown in red symbols, while those observed on F-type stars with masses in the range  $1.15$ – $1.25 M_{\odot}$  are shown as diamonds,  $1.25$ – $1.35 M_{\odot}$  as triangles, and  $1.35$ – $1.45 M_{\odot}$  as squares. Observational data are from Table B.1 of Reiners (2006).

(A color version of this figure is available in the online journal.)

Collier Cameron et al. 2002; Silva-Valio & Lanza 2011), and asteroseismology (e.g., Thompson et al. 1996; Schou et al. 1998; Verner et al. 2011). For the F-type stars, a Fourier analysis technique using stellar spectra has produced the largest number of detections of differential rotation to date (Reiners 2007). In this method, many spectral lines from a target star are averaged to produce a mean line profile, which is then Fourier transformed. The ratio of the first two minima, which are denoted as  $q_1$  and  $q_2$ , of the resulting power spectrum of this line is used to determine whether or not the star is differentially rotating, and if so by how much.

In Figure 1, the upper bound of the absolute differential rotation of F-type stars increases with rotation rate, where it may reach a plateau or even slightly decrease at higher rotation rates (Reiners 2006). However, the current paucity of accurate observational data makes it difficult to establish robust trends. In Figure 1, we have only shown stars with masses between  $1.15$  and  $1.45 M_{\odot}$  that have a measurement of both the differential rotation and its uncertainty. It is likely, however, that rather more of the stars in Reiners (2006) actually rotate differentially as it is difficult to detect when a star rotates too rapidly or too slowly. Indeed, stars with a projected rotational velocity ( $v \sin i$ ) greater than  $50 \text{ km s}^{-1}$  have a relative differential rotation that often falls below the detection threshold. Similarly, when using the method of Reiners & Schmitt (2002), stars with  $v \sin i \leq 10 \text{ km s}^{-1}$  rotate too slowly to accurately measure the bulk rotation rate, further restricting the range of detection. Those stars identified as differentially rotating exhibit a wide range of relative differential rotation. There is even the suggestion that several stars may possess anti-solar differential rotation, where the pole rotates more rapidly than the equator, and which may also be interpreted as cool polar spots.

There appears to be a trend in the observations of Reiners (2006) in which the number of stars that rotate differentially seems to decrease with increasing mass and thus decreasing  $B - V$  color. However, this could be a two fold selection effect. The first effect is from the non-uniform color (effective

**Table 1**  
Properties of Cases A and B

Cases	$M$	$L$	$R$	$T_{\text{eff}}$	$\log_{10} g$	$r_1/R$	$r_2/R$
A	1.20	2.00	1.19	6300	4.54	0.80	0.98
B	1.30	2.93	1.33	6540	4.48	0.86	0.98

**Notes.** The mass of the star being simulated ( $M$ ) is given in units of  $M_{\odot}$  ( $1.98 \times 10^{33} \text{ g}$ ), luminosity ( $L$ ) in units of  $L_{\odot}$  ( $3.86 \times 10^{33}$ ), stellar radius ( $R$ ) in units of  $R_{\odot}$  ( $6.96 \times 10^{10} \text{ cm}$ ), the stellar effective temperature ( $T_{\text{eff}}$ ) in kelvin, and the logarithm of gravity in  $\text{cm s}^{-2}$ . The lower and upper radial boundaries of the simulation domains are in turn  $r_1$  and  $r_2$ .

temperature) sampling of stars. The distribution is roughly Gaussian between  $B - V$  values of 0.2 and 0.6, or spectral types A7 and G1, respectively, with a peak at a  $B - V$  of 0.4 (spectral type F4). The second effect arises from the fact that higher mass stars tend to rotate more rapidly and thus their  $q_2 - q_1$  values fall below the differential rotation detection threshold. Of the stars that do rotate differentially, the results for the F-type stars with the largest differential rotation in Reiners (2006) are consistent with the trend of increasing absolute differential rotation found (Barnes et al. 2005; Collier Cameron 2007), in which it is found that absolute differential rotation increases strongly with effective temperature or increasing mass. This seems to be the case in our simulations as well (see Figure 1 and Section 8).

### 1.3. Global Models of F-type Star Convection

How the angular momentum in a star is redistributed to produce and maintain a stable angular velocity profile appears to involve subtle dynamical balances. The highly turbulent nature of stellar convection coupled with rotation involves a vast range of scales, making it quite challenging to directly model such dynamic processes. Yet these issues must be explored if the behavior of stellar rotation is to be understood. Rapid advances in supercomputing have enabled global-scale three-dimensional (3D) simulations of convection coupled with rotation that are shedding light on the dynamics of the flow achieved within stars (Bessolaz & Brun 2011; Brown et al. 2008; Miesch et al. 2008). In a similar spirit, we are reporting on the dynamics of turbulent global-scale convection in a realistically stratified computational domain in two main-sequence F-type stars that are each studied over a range of rotation rates. The two stars investigated here are a  $1.2 M_{\odot}$  star (Case A simulations) and a  $1.3 M_{\odot}$  star (Case B simulations) that possess the same central hydrogen abundance, resulting in main-sequence ages of 1.15 Gyr and 1.00 Gyr, respectively (see Table 1). As mentioned above, convection zone depth and luminosity change rapidly with mass in F-type stars. Indeed, the tenth of a solar mass difference between the two stars simulated here leads to a 50% increase in luminosity and a 50% decrease in convection zone depth, allowing us to also probe how the vigor of the convection and convection zone geometry impact the mean properties of the flows established in these stars.

In our analysis of these simulations, we first provide details about the anelastic equations solved, the formulation of the numerics, and the setup of the numerical experiments in Section 2. The general properties of the convective patterns and mean flows of selected cases are discussed in Section 3. We look at the dynamics in detail for a particular case in Section 4. The effects of overshooting convection are addressed in Section 5. The link between the thermal properties of the simulations and the differential rotation is probed in Section 6. The connection between the two mean flows, the differential rotation and the meridional

circulation, is examined for these two cases in Section 7. Finally, in Section 8, the scaling of the magnitudes of the mean flows and the thermal signatures of the flows are presented.

## 2. FORMULATING THE PROBLEM

The convection zones of most stars are extremely turbulent with very small values of viscosity and thermal diffusivity. A direct numerical simulation that effectively captures all of the relevant scales of motion in a stellar convection zone is currently, and for the foreseeable future, impossible. Therefore, a model that eliminates the fast timescales of sound waves and parameterizes the dynamics at small spatial scales is necessary in order to capture the large number of rotational periods and the full spherical geometry. Such features are thought to be crucial in establishing an equilibrium state that maintains a differential rotation. To this end, we use the 3D anelastic spherical harmonic (ASH) simulation code. ASH is a mature modeling tool that solves the anelastic MHD equations of motion in a rotating spherical shell using a pseudospectral method. ASH simulations capture the entire spherical shell geometry and allow for zonal jets, large-scale vortices, and structures with connectivity such as convective plumes. The simulated turbulence is still many orders of magnitude removed from the intensely turbulent conditions present in stellar convection zones. Despite this discrepancy, simulations of the solar convection zone using ASH have been successful in matching helioseismic constraints on differential rotation within the solar convection zone (Miesch et al. 2000, 2006, 2008; Brun & Toomre 2002; Brun et al. 2011).

### 2.1. Anelastic Equations

In the anelastic approximation, the time derivative of the density in the continuity equation is eliminated. This approximation is employed to capture the effects of density stratification without having to resolve the rapidly varying sound waves. In this approximation, the Courant–Friedrichs–Lewy condition on the time step will then be governed by the subsonic flow velocity rather than the sound speed. The anelastic equations evolved within ASH are fully nonlinear in the velocity variables, but the thermodynamic variables are linearized about the spherically symmetric and evolving mean stratification composed of the quantities  $\bar{\rho}$ ,  $\bar{S}$ ,  $\bar{P}$ , and  $\bar{T}$  for the density, entropy, pressure, and temperature, respectively. The fluctuations of thermodynamic variables are taken about the mean stratification and are denoted as  $\rho$ ,  $S$ ,  $P$ , and  $T$ . These fluctuations are generally of the order  $\epsilon = (\gamma - 1) M^2$ , where  $M$  is the Mach number of the flow at a given depth, which in the simulations here gives  $\epsilon \approx 10^{-6}$ . The resulting equations in physical units, in spherical coordinates  $(r, \theta, \phi)$ , and with time  $t$  are (Glatzmaier 1984; Clune et al. 1999)

$$\begin{aligned} \bar{\rho} \frac{\partial \mathbf{u}}{\partial t} = & -\bar{\rho} \mathbf{u} \cdot \nabla \mathbf{u} - \nabla P - \rho \mathbf{g} \\ & + 2\bar{\rho} \mathbf{u} \times \hat{\Omega}_0 + \nabla \cdot \mathcal{D} - \Lambda \hat{\mathbf{r}}, \end{aligned} \quad (1)$$

$$\bar{\rho} \bar{T} \frac{\partial S}{\partial t} = -\bar{\rho} \bar{T} \mathbf{u} \cdot \nabla (\bar{S} + S) - \nabla \cdot \mathbf{q} + \Phi, \quad (2)$$

$$\frac{\partial \bar{P}}{\partial r} = -\bar{\rho} g_r + \Lambda, \quad (3)$$

$$\nabla \cdot \bar{\rho} \mathbf{u} = 0, \quad (4)$$

where  $\mathbf{u} = u_r \hat{\mathbf{r}} + u_\theta \hat{\boldsymbol{\theta}} + u_\phi \hat{\boldsymbol{\phi}}$  is the velocity vector,  $\hat{\Omega}_0 = \Omega_0 \hat{\mathbf{z}}$  is the angular velocity of the rotating frame,  $\hat{\mathbf{z}}$  is the axial

unit vector, and  $c_p$  is the specific heat at constant pressure. The gravitational acceleration is taken to be  $\mathbf{g} = -g(r) \hat{\mathbf{r}}$ . As the simulation evolves, a turbulent pressure pushes the system slightly away from the initial hydrostatic equilibrium;  $\Lambda$  in Equation (3) is the radial gradient of the spherically symmetric component of this turbulent pressure. The components of the viscous stress tensor  $\mathcal{D}$  are Newtonian and  $\Phi$  is the viscous heating, which are given by

$$\mathcal{D}_{ij} = 2\bar{\rho} \nu \left[ e_{ij} - \frac{1}{3} \nabla \cdot \mathbf{u} \delta_{ij} \right], \quad (5)$$

$$\Phi = 2\bar{\rho} \nu \left[ e_{ij} e_{ij} - \frac{1}{3} (\nabla \cdot \mathbf{u})^2 \right], \quad (6)$$

where  $e_{ij}$  is the stress tensor and  $\nu$  is the effective kinematic viscosity. The energy flux  $\mathbf{q}$  is composed of two diffusive components,

$$\mathbf{q} = \kappa_r \bar{\rho} c_p \nabla (\bar{T} + T) + \kappa \bar{\rho} \bar{T} \nabla S + \kappa_0 \bar{\rho} \bar{T} \frac{\partial \bar{S}}{\partial r} \hat{\mathbf{r}}, \quad (7)$$

where the first component is a radiation diffusion flux with the molecular radiation diffusion coefficient  $\kappa_r$ . The second component is an anisotropic entropy diffusion flux, with  $\kappa$  acting on the non-axisymmetric entropy fluctuations and another  $\kappa_0$  acting only on the spherically symmetric component of the entropy. The form and impact of these diffusive transport coefficients are discussed in Section 2.3.

Ideally, the system would adjust to a new equilibrium by modifying the Rosseland mean opacity and the thermal stratification. The overshooting convection realized in our simulations modifies the mean stratification in the overshooting region. However, to fully adjust the mean thermal state, and thus the radiative flux, would require evolving the simulation for a thermal relaxation time. This timescale is about  $E_i/L \approx 2400$  yr for the  $1.2 M_\odot$  F-type stars and about 160 yr for the  $1.3 M_\odot$  F-type stars, where  $E_i$  is the total internal energy of the plasma in the stable region and  $L$  is the luminosity. Since achieving these timescales is currently beyond our computational resources, we accelerate this process by first simulating the stars with the Rosseland mean opacity ( $\kappa_{\text{Ros}}$ ) and the 1D thermodynamic state from the stellar model and then updating this opacity using the evolved thermodynamic state of the simulation. This is accomplished by Taylor expanding the opacity using the partial derivatives of the opacity with respect to the density and temperature extracted from the stellar model and then updating the radiative diffusion coefficient with the mean thermal state as

$$\begin{aligned} \kappa'_{\text{Ros}} = & \kappa_{\text{Ros}}^0 + \left. \frac{\partial \kappa_{\text{Ros}}}{\partial \rho} \right|_0 (\bar{\rho} - \bar{\rho}_0) + \left. \frac{\partial \kappa_{\text{Ros}}}{\partial T} \right|_0 (\bar{T} - T_0), \\ \kappa_r = & \frac{4ac\bar{T}^3}{3c_p \bar{\rho}^2 \kappa'_{\text{Ros}}}, \end{aligned}$$

where the subscript 0 indicates that these quantities are taken from the stellar model. This scheme is typically applied only once but can be used as frequently as necessary to achieve an equilibrium. Updating the diffusion coefficient in this fashion ensures that the radiative energy flux and the enthalpy flux are properly balanced in the stable region, providing for a nearly constant total flux throughout the domain and also avoiding the long-time evolution that would otherwise be required (see Section 4.2). Finally, a linearized equation of state closes the set

of equations for the fluctuations, while the ideal gas law closes the equations for the mean state:

$$\rho/\bar{\rho} = P/\bar{P} - T/\bar{T} = P/\gamma\bar{P} - S/c_P, \quad (8)$$

$$\bar{P} = (\gamma - 1)c_P\bar{\rho}\bar{T}/\gamma, \quad (9)$$

where  $\gamma$  is the adiabatic exponent. A stellar evolution code, MESA (Paxton et al. 2011), is employed to evolve a realistic 1D stellar model at the solar metallicity and helium mass fraction from the pre-main sequence to a central hydrogen mass fraction of 0.54. This places these models at about 20% of their main-sequence lifetime. This model is then used to establish the initial mean stratification for an ASH simulation. For the numerical experiments conducted here, we neglect the effects of stellar evolution. A single initial stellar structure model is used for each of the two simulated F-type stars shown in Table 1.

## 2.2. Numerics and Experimental Configuration

In the ASH code, the mass flux remains divergence free through a poloidal–toroidal stream function decomposition. These stream functions and the variations in the entropy and pressure are expanded in spherical harmonics  $Y_\ell^m(\theta, \phi)$ , with spherical harmonic degree  $\ell$  and azimuthal order  $m$ , to resolve their horizontal structures and in Chebyshev polynomials  $T_n(r)$  to resolve their radial structures. Temporal discretization is accomplished using a semi-implicit Crank–Nicolson time-stepping scheme for linear terms and an explicit Adams–Bashforth scheme for nonlinear terms. ASH is designed with modern programming constructs to yield efficient performance and scaling on massively parallel supercomputers (e.g., Clune et al. 1999). Several codes numerically solving for anelastic magnetohydrodynamics, including ASH, have recently been thoroughly tested on the same suite of nonlinear problems in which the accuracy of several numerical methods has been probed extensively and shown to be robust (Jones et al. 2011).

The studies here explore a range of rotation rates for each mass, from  $5 \Omega_\odot$  to  $20 \Omega_\odot$  for the  $1.2 M_\odot$  *Case A* simulations and from  $8 \Omega_\odot$  to  $30 \Omega_\odot$  for the  $1.3 M_\odot$  *Case B* simulations. All cases at a given mass use the same initial stellar structure and are initialized with random perturbations in the fluctuating entropy. These ranges of rotation rates are chosen so that all the cases exhibit solar-like differential rotation, where the poles rotate more slowly than the equator, as is discussed in Section 8. Note that the nomenclature for the cases is *Case A* or *Case B* depending on the mass followed by the bulk rotation rate quoted in integer multiples of the solar rotation rate. So, *Case A10* is a  $1.2 M_\odot$  F-type star rotating at 10 times the solar rate. Cases that omit the stable layer, simulating only the convectively unstable region, are denoted with an *i* after the case’s name.

While most parameters and the initial stratification are taken from the stellar model, a perfect gas is assumed (Equation (9)). Therefore, the He and H ionization zones that occur in the outer 1% by radius of these stars cannot be properly captured. Additionally, ionization coupled with radiative losses drives very intense convection on small scales. These small-scale flows are nearly sonic, so sound waves play an important role in the dynamics and cannot be neglected. Thus, the radius of the upper boundary ( $r_2$ ) in our simulations is taken to be below this region, where the Mach number is generally very small, so that the assumptions made in the formulation of the anelastic approximation remain valid.

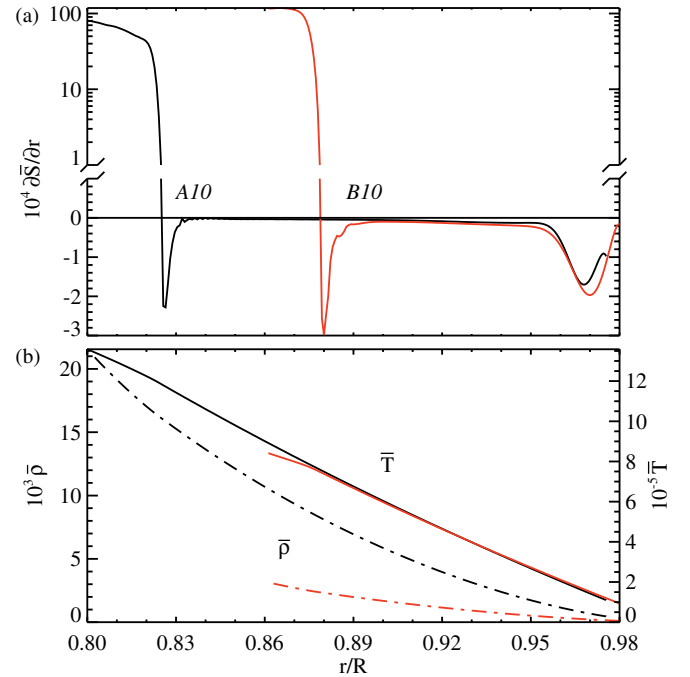


**Figure 2.** Time-averaged mean stratification established in *Case A10* (black lines) and *Case B10* (red lines). (a) The entropy gradient ( $\partial \bar{S} / \partial r$  in units of  $10^{-4} \text{ erg cm}^{-4} \text{ K}^{-1}$ ); the break in the y-axis denotes the change from linear to logarithmic scaling. (b) The density ( $\bar{\rho}$  in units of  $10^{-3} \text{ g cm}^{-3}$ , dash-dotted line) and temperature ( $\bar{T}$  in units of  $10^5 \text{ K}$ , solid line).

(A color version of this figure is available in the online journal.)

The simulations being reported on here include a portion of the stable radiative zone below the convection zone as seen in Figure 2, in a manner similar to the simulations that have been carried out in a solar setting in Browning et al. (2006) and Brun et al. (2011). Such a layer has been shown to play a large role in determining the radial and latitudinal structure of the differential rotation (Rempel 2005). Indeed, the dependence of the morphology of the differential rotation on the amplitude of a weak latitudinal entropy gradient imposed at an impenetrable lower boundary has been explored within ASH simulations of the Sun. The simulations in Miesch et al. (2006) use this latitudinal entropy gradient to emulate a tachocline that is in a thermal wind balance. It was found that this gradient spurred an adjustment of the contours of constant angular velocity from an alignment with the rotation axis to a radial alignment. The impetus behind these various efforts is to understand why the helioseismically determined angular velocity of the Sun has nearly conical contours (Schou et al. 1998), as is also found in the angular velocity contours of the simulations explored here (see Sections 3.1 and 3.2).

The position of the radius of the lower boundary ( $r_1$ ) is determined by how deep the overshooting motions occurring within the simulations penetrate into the stable zone and by how much resolution is necessary to fully resolve the steep entropy gradient that arises below the convection zone. The radial extent of the stable region in these simulations is set to be roughly twice the penetration depth of the overshooting motions. This choice reduces the need for a high radial resolution and allows these simulations to capture the effects that convective overshooting and a stable layer have on the mean flows and thermodynamic properties of the convection. However, it does restrict the ability of the simulations to capture the full spectrum of gravity waves

excited by the convection as some of the modes are trapped within this cavity (see Brun et al. 2011).

### 2.3. Diffusion and Sub-grid-scale Models

The anelastic system of hydrodynamic equations requires eight boundary conditions in order to be well posed. One of the primary goals of this work is to assess the redistribution of angular momentum and energy in our simulations. Thus, we have opted for the following torque-free and flux-transmitting boundary conditions:

$$u_r = \frac{\partial}{\partial r} \left( \frac{u_\theta}{r} \right) = \frac{\partial}{\partial r} \left( \frac{u_\phi}{r} \right) = \frac{\partial S}{\partial r} \Big|_{r_2, r_1} = 0, \quad (10)$$

where the constant flux boundary condition on the entropy fluctuations implies that the mean entropy gradient remains unchanged on the boundaries throughout the simulation. The stress-free boundary conditions used in the simulations here ensure that the volume-integrated transport terms nearly vanish. Indeed, the total angular momentum is conserved to within the global accuracy of the radial derivatives at each time step. Over the course of the entire simulation where the mean stratification is allowed to change, it is conserved to within the order  $\epsilon$ , roughly the order to which the anelastic approximation is valid.

Current and foreseeable computing resources render simulations that directly capture all scales of stellar convection from global to molecular dissipation scales unattainable. The simulations reported on here resolve nonlinear interactions among a large range of scales in both the convective and radiative zones of two F-type stars. Motions and waves within the actual star exist on scales smaller than our grid resolution, and in this sense our models should be regarded as large-eddy simulations (LESs). These sub-grid-scale motions are parameterized as effective viscous and thermal diffusivities ( $\nu$  and  $\kappa$ , respectively), which are meant to emulate the mixing properties of the unresolved turbulent eddies. The anisotropic diffusion treatment comes from our separation of the  $\ell = 0$  component of the energy equation, from higher order spherical harmonic modes. The second term in Equation (7) involving  $\kappa$  is a sub-grid-scale diffusion that acts on the  $\ell > 0$  components of the entropy fluctuations. The term in Equation (7) with  $\kappa_0$  is a sub-grid-scale transport acting on the mean entropy gradient and the  $\ell = 0$  entropy fluctuations in an isolated upper portion of the domain. This term ensures that the full stellar luminosity is carried through the upper boundary by conduction. This term can alternatively be thought of as a cooling near the surface. This anisotropic formulation has been used in most prior work employing the ASH code (e.g., Brown et al. 2008, 2010; Brun et al. 2011). It also allows the simulations to relax more rapidly and provides better convergence characteristics. Most importantly, it allows the convection to dominate the radial energy transport in the bulk of the domain. We have found that this anisotropic diffusion model has little impact on the resulting flows and mean properties of the more rapidly rotating simulations.

These diffusivities are allowed to vary in radius only and evolve slowly in time as they are dependent on the profile of the mean density  $\bar{\rho}$ . The radial profiles of  $\nu$ ,  $\kappa$ , and  $\kappa_0$  are given by

$$f(r; a, b) = \{1 + \exp[a(b - r)/(r_2 - r_1)]\}^{-1}, \quad (11)$$

$$\nu(r) = \nu_{\text{top}} \left( \frac{\bar{\rho}}{\bar{\rho}_{\text{top}}} \right)^{-1/2} f(r; \alpha, r_\nu) + \nu_{\text{min}}, \quad (12)$$

$$\kappa(r) = \kappa_{\text{top}} \left( \frac{\bar{\rho}}{\bar{\rho}_{\text{top}}} \right)^{-1/2} f(r; \alpha, r_\kappa) + \kappa_{\text{min}}, \quad (13)$$

$$\kappa_0(r) = \kappa_0^{\text{top}} \exp[-\beta(r_2 - r)/(r_2 - r_1)] f(r; \delta, r_{\kappa_0}) + \kappa_0^{\text{min}}, \quad (14)$$

where  $\kappa_{\text{top}}$  is the thermal diffusivity at the upper boundary,  $\kappa_{\text{min}}$  is the floor value of this diffusivity, and  $\alpha$  controls the steepness of the tapering function  $f(r; \alpha, r_\nu)$  below a particular radius  $r_\nu$ . This allows the diffusion to be greatly reduced in stable regions, where motions have a small amplitude and the expected sub-grid-scale motions are subsequently smaller. The Prandtl number is  $\text{Pr} = \nu/\kappa = 1/4$  and is fixed throughout the domain, so  $\nu = \text{Pr}\kappa$ . In both the *Case A* and *Case B* simulations,  $\alpha = 300$  and the minimum levels of diffusion  $\nu_{\text{min}}$  and  $\kappa_{\text{min}}$  are set to be 1000 times smaller than  $\nu_{\text{top}}$  and  $\kappa_{\text{top}} = \nu_{\text{top}}/\text{Pr}$ , with  $\nu_{\text{top}}$  given in Table 2. The radius below which the diffusion drops rapidly is  $r_\kappa = r_\nu = 6.7 \times 10^{10}$  cm for *Case A* simulations and  $r_\kappa = r_\nu = 8 \times 10^{10}$  cm for *Case B* simulations. The diffusion acting on the mean entropy has the coefficient  $\kappa_0$ , which is set so that this unresolved eddy flux carries the stellar luminosity through the upper boundary but is exponentially tapered with depth below  $r_2$ . It is further quenched below the radius  $r_{\kappa_0}$ , with the rapidity of the decrease controlled by  $\delta$ . This allows the convective motions to carry the majority of the flux throughout the convection zone and avoids an inward diffusive energy flux in sub-adiabatic regions. In the *Case A* simulations,  $\kappa_0^{\text{top}} = 1.91 \times 10^{13} \text{ cm}^2 \text{ s}^{-1}$ ,  $\beta = 60$ ,  $\delta = 200$ , and  $r_{\kappa_0} = 6.95 \times 10^{10}$  cm, while in the *Case B* simulations  $\kappa_0^{\text{top}} = 6.67 \times 10^{14} \text{ cm}^2 \text{ s}^{-1}$ ,  $\beta = 100$ ,  $\delta = 200$ , and  $r_{\kappa_0} = 8.22 \times 10^{10}$  cm.

The unresolved eddy diffusion associated with the spherically symmetric diffusion component acts to conduct the full stellar flux through the upper boundary. Thus, almost by definition it has a substantial influence on the spherically symmetric component of the entropy. The monotonically decreasing initial entropy gradient from the stellar model is significantly steepened near the upper boundary by the cooling induced by the unresolved eddy flux, as is clearly seen as a large dip near the upper boundary in Figure 2. This has the effect of enhancing the buoyancy driving in the upper convection zone relative to what might be expected if the upper boundary were open and the surface convection allowed to influence the deeper flows. Recent 3D surface convection simulations have shown a sizable change in the entropy gradient in the surface layers of various stars when compared to the gradient expected from standard mixing-length theory (Trampedach & Stein 2011). While the total integrated entropy deficit across the convection zone remains the same, as the luminosity is the same, its radial distribution is somewhat different. The gradient of the entropy becomes more superadiabatic near the surface and more adiabatic in the bulk of the convection zone. Therefore, the total entropy contrast across the domain in these simulations may be too high relative to the actual stratification, especially in simulations at lower rotation rates where the steepest superadiabatic gradients arise. This results in flows that begin to feel the effects of rotation at depths greater than otherwise might occur. The transition between flows that strongly feel the bulk rotation and those that do not takes place where the fluctuating Rossby number of the flows drops below one. Thus, we attempt to temper the influence of the upper boundary on the dynamics of the interior by ensuring that the fluctuating Rossby number throughout the convection

**Table 2**  
Diagnostic Flow Parameters

Mass	Case	$\Omega_0/\Omega_\odot$	$N_r \times N_\theta \times N_\phi$	Ra	Ta	Re	Re'	Ro	Ro'	RoDR	Ro <sub>mc</sub>	$\nu_{\text{top}}$	$\tau_c$	$\tau_\nu$
1.2 $M_\odot$	A5	5	$257 \times 512 \times 1024$	$1.75 \times 10^5$	$2.40 \times 10^5$	84	37	0.69	0.48	0.29	0.017	2.52	2.8	101
	A7	7	$257 \times 512 \times 1024$	$2.62 \times 10^5$	$7.36 \times 10^5$	140	44	0.52	0.35	0.24	0.014	2.01	3.0	126
	A10	10	$257 \times 512 \times 1024$	$4.22 \times 10^5$	$2.41 \times 10^6$	240	52	0.39	0.25	0.21	0.008	1.59	3.3	159
	A15	15	$257 \times 512 \times 1024$	$7.64 \times 10^5$	$9.32 \times 10^6$	451	75	0.28	0.18	0.19	0.004	1.21	3.7	209
	A20	20	$257 \times 512 \times 1024$	$1.60 \times 10^6$	$2.42 \times 10^7$	644	102	0.25	0.15	0.16	0.004	1.00	3.9	252
	A5 <i>i</i>	5	$97 \times 512 \times 1024$	$1.22 \times 10^5$	$2.29 \times 10^5$	82	38	0.63	0.44	0.23	0.016	2.52	3.2	96
	A20 <i>i</i>	20	$97 \times 512 \times 1024$	$1.04 \times 10^6$	$2.30 \times 10^7$	410	76	0.23	0.14	0.14	0.002	1.00	4.2	241
1.3 $M_\odot$	B8	8	$193 \times 512 \times 1024$	$4.32 \times 10^4$	$9.21 \times 10^4$	62	41	0.99	0.73	0.07	0.021	3.20	1.1	39
	B10	10	$193 \times 512 \times 1024$	$6.45 \times 10^4$	$1.90 \times 10^5$	108	44	0.84	0.61	0.11	0.012	2.78	1.2	44
	B15	15	$193 \times 512 \times 1024$	$1.19 \times 10^5$	$7.34 \times 10^5$	207	57	0.56	0.40	0.12	0.009	2.12	1.3	59
	B20	20	$193 \times 512 \times 1024$	$2.34 \times 10^5$	$1.91 \times 10^6$	363	76	0.46	0.31	0.13	0.009	1.75	1.5	71
	B30	30	$193 \times 512 \times 1024$	$4.25 \times 10^5$	$4.31 \times 10^6$	324	73	0.28	0.19	0.09	0.004	1.75	1.7	71
	B20 <i>i</i>	20	$97 \times 512 \times 1024$	$9.49 \times 10^4$	$1.43 \times 10^6$	248	58	0.51	0.30	0.21	0.001	1.75	1.5	60

**Notes.** The depth of the convection zone ( $d = r_2 - r_b$ , where  $r_b$  is the radius of the bottom of the convection zone) is the relevant length scale in the following parameters and is  $1.3 \times 10^{10}$  cm for *Case A* simulations and  $9.2 \times 10^9$  cm for *Case B* simulations. We estimate and quote the following diagnostic parameters at mid-convection zone: the Rayleigh number  $Ra = \Delta \bar{S} g d^3 / c_p \nu \kappa$ , Taylor number  $Ta = 4 \Omega_0^2 d^4 / \nu^2$ , Reynolds number  $Re = v_{\text{rms}} d / \nu$ , fluctuating Reynolds number  $Re' = v'_{\text{rms}} d / \nu$ , Rossby number  $Ro = |\bar{\omega}| / 2 \Omega_0$ , and fluctuating Rossby number  $Ro' = |\bar{\omega}'| / 2 \Omega_0$ , where  $\langle \rangle$  denotes a horizontal average and  $\omega$  is the vorticity vector. The differential rotation and meridional circulation Rossby numbers at mid-convection are  $Ro_{\text{DR}} = |\bar{\lambda} \nabla \ln \Omega|$  and  $Ro_{\text{mc}} = |\bar{\omega}_\phi| / 2 \Omega_0$ , respectively. The bar denotes the horizontal average. Kinematic viscosity ( $\nu$ ) values are given in units of  $10^{13}$  cm<sup>2</sup> s<sup>-1</sup>. The mid-convection zone local overturning time  $\tau_c$  and the viscous diffusion time  $\tau_\nu$  across the convection zone are quoted in days. Case labels are as in Section 2.2, where an *i* indicates an impenetrable lower boundary.

zone is less than one. This requires that the rotation rate be high enough to attain  $Ro' < 1$ , as is the case for the simulations here as indicated in Table 2.

#### 2.4. Scaling Diffusion with Rotation

In the Boussinesq approximation, convection becomes possible above a critical Rayleigh number, which scales with rotation rate as  $Ra_c \propto \Omega_0^{4/3}$  (e.g., Chandrasekhar 1961; Dormy et al. 2004). Anelastic systems have a similar constraint on the minimum Rayleigh number that is necessary for the flows to be convective (Glatzmaier & Gilman 1981; Jones et al. 2009). We seek here to explore the effects of rotation on stellar convection in the global spherical geometry at a representative point of time within the main-sequence lifetime of these two F-type stars. This goal means that the simulations must be highly supercritical so that the level of turbulence dominates diffusion. With unlimited computer resources, we ideally would maintain a constant level of supercriticality, but this requires scaling the effective diffusivities  $\nu$  and  $\kappa$  as  $\Omega_0^{-2}$ . However, lower diffusivities lead both to longer viscous and thermal diffusion timescales and to flows possessing finer spatial scales. Achieving equilibrated states in these systems requires high-resolution simulations carried out over extended periods, which would be prohibitively expensive if we followed this path. We have attempted to balance the level of supercriticality and the resolution requirements necessary to resolve the flow in our path through parameter space. Thus, our trajectory through the parameter space of  $\Omega_0$ ,  $\nu$ , and  $\kappa$  attempts to maintain strongly nonlinear dynamics without the increased rotation rate laminarizing the convection. In our simulations, we have constrained this trajectory to be 1D by requiring that the Prandtl number be 1/4 and that the value  $\nu_{\text{top}}$  be set relative to the most rapidly rotating case and subsequently scaled according to  $\nu_{\text{top}} \propto \Omega_0^{-2/3}$ , as seen in Table 2.

The Rayleigh numbers at mid-convection zone are about 50 times the critical Rayleigh number (Jones et al. 2009) for the *Case A* simulations and about 25 times for the *Case B* simulations. These levels of supercriticality are equivalent to

ASH simulations of lower mass stars (e.g., Brown et al. 2008; Matt et al. 2011). The lower level of supercriticality in the 1.3  $M_\odot$  simulations is primarily due to the stronger driving of the convection and larger superadiabatic gradient, both of which are in turn due to the higher luminosity and narrower convection zones of the higher mass F-type stars. This requires that the diffusion in the *Case B* simulations be about two times larger than the lower mass *Case A* simulation at the same rotation rate. This is done to ensure numerical stability at a chosen resolution as the downflows tend to be faster with larger temperature deficits in *Case B* simulations due to the higher luminosity of the star. The radial extent of the convection zone is taken to be the representative scale for determining the flow parameters seen in Table 2. This, in combination with a larger diffusion, results in lower Reynolds and Rayleigh numbers for *Case B* simulations. As a matter of definition, an evolved case is one in which the volume-averaged differential rotation and kinetic energies vary by less than 0.1% relative to an initial value over a span of about 1000 days of simulation time. The differential rotation and other quantities are measured in these evolved cases to ensure that the time averages taken are essentially stationary.

### 3. CONVECTIVE PATTERNS AND MEAN STRUCTURE

The variation of convective patterns of selected *Case A* simulations with increasing rotation rate  $\Omega_0$  is illustrated in the first column of Figures 3(a), (e), and (i), while the same is shown for three *Case B* simulations in Figure 4. These snapshots of the radial velocity near the top of the domain (0.96  $R$ ) are shown in Mollweide projection for three cases in Figure 3: *Case A5*, *Case A10*, and *Case A20*. The radial velocities exhibit the complex, evolving, and global-scale nature of the convection established in these simulations. The convective cells that compose these complex patterns are outlined by the dark downflows. A distinctive transition in the morphology of the convective cells occurs between the columnar equatorial cells, which are essentially viewed from the side given the spherical geometry, and the polar columns, where they are viewed from the top down. Equatorial convective columns march around the

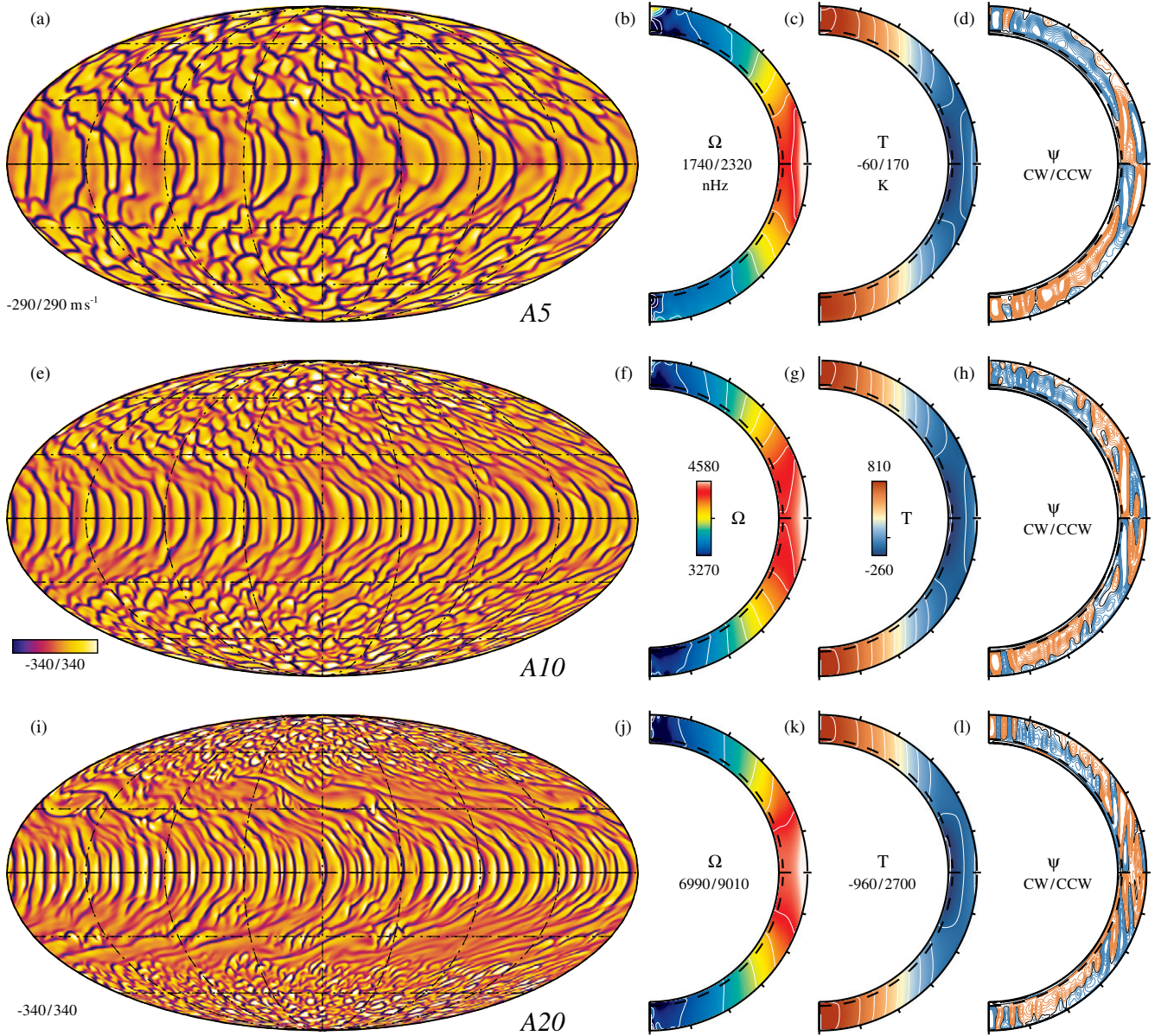


**Figure 3.** Overview of convective patterns, mean flows, and mean temperature fluctuations in selected *Cases A*. (a, e, i) The first column of the figure displays convective patterns in radial velocities near the upper boundary in turn for *Case A5*, *Case A10*, and *Case A20*. (b, f, j) The second column presents the time-averaged and azimuthally averaged angular velocity with radius and latitude, with the fast prograde equator in red and slower poles in blue. (c, g, k) Azimuthally averaged and time-averaged temperature fluctuations (where the  $\ell = 0$  component has been removed) with the warm poles in red tones and the cool equator in blue tones. (d, h, l) The stream function of the meridional flow ( $\psi$ ), clockwise (CW) flows in red, and counterclockwise (CCW) flows in blue. The dashed line in the second, third, and fourth columns delineates the beginning of the stable region.

(A color version of this figure is available in the online journal.)

equator in a prograde sense, constantly jockeying for position as they collide and overtake one another. Cells of convection at higher latitudes continually form and reform as they interact with one another and are shuffled along by the mean flows in a retrograde sense. The mean zonal flow makes its presence felt at mid-latitudes, where there is an obvious shear between the prograde equatorial flows and the retrograde polar flows. These flows exhibit somewhat different timescales over which they maintain their coherence. The convective cells at the poles can last a few days, and those at the equator last even longer.

### 3.1. Case A: $1.2 M_{\odot}$ Simulations

In Figure 3, there is a juxtaposition between high and low latitudes in both the scale and structure of the convection, especially for more rapidly rotating cases. The latitudinal

variation of convection patterns can be in part understood by considering a cylinder tangent to the base of the convection zone whose axis of symmetry is aligned with the rotation axis. Within the geometry of the *Case A* simulations, the top of such a cylinder intersects the upper boundary at latitudes of  $\pm 32^{\circ}$ . Outside the tangent cylinder, downflows are deflected equatorward by Coriolis forces and can connect across the equator before they are strongly braked in the stable region. For downflows inside the tangent cylinder, they generally encounter the stable region before they can be paired with a flow from the opposite hemisphere. Such constraints on the convection become more severe as the rotation rate of the frame is increased.

The flows outside the tangent cylinder organize into large-scale sheared cylindrical rolls aligned with the rotation axis. Individual convective cells remain coherent for roughly the

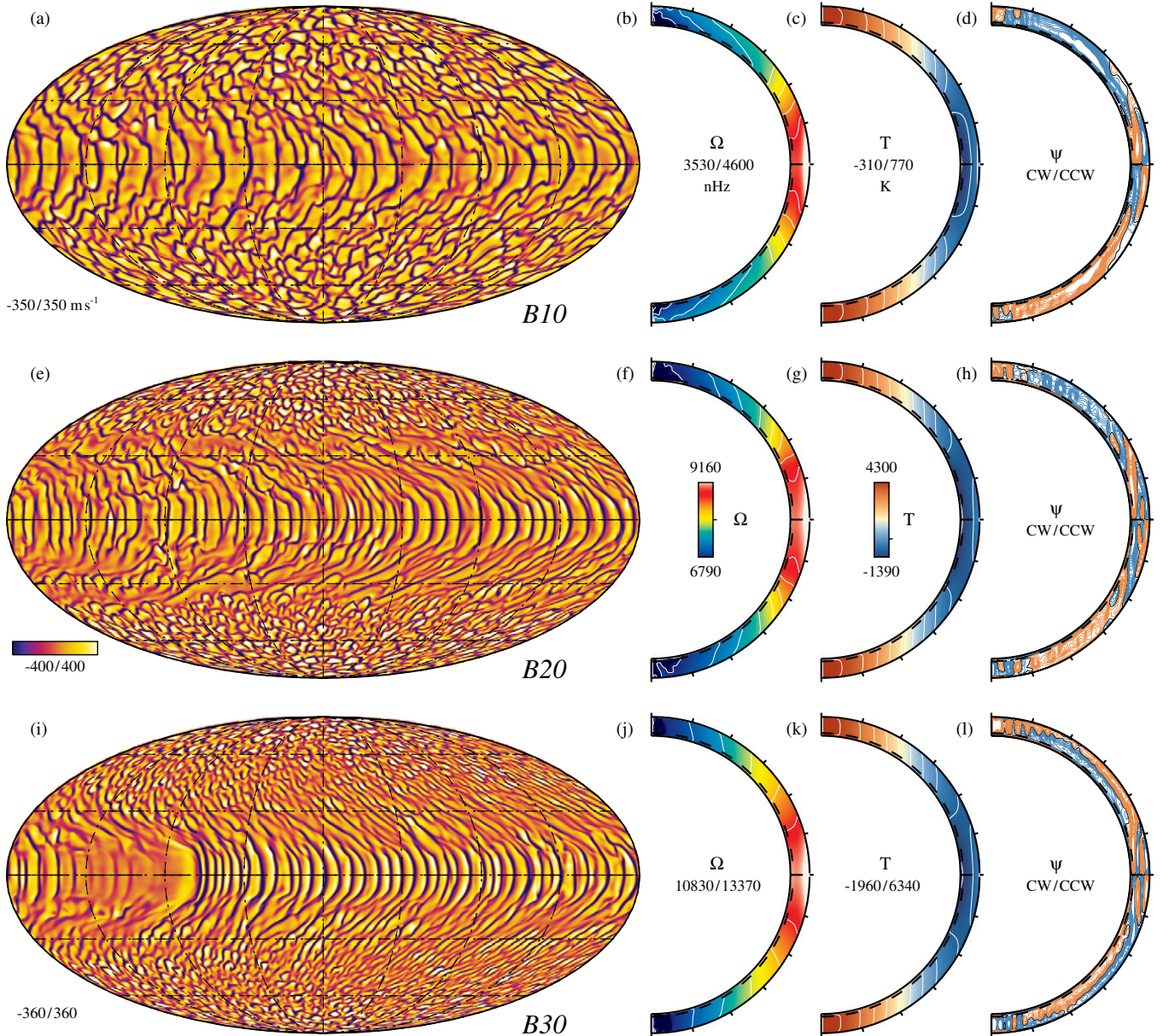


**Figure 4.** Overview of convective patterns, mean flows, and mean temperature fluctuations in selected *Cases B*. (a, e, i) The first column of the figure displays convective patterns in radial velocities near the upper boundary in turn for *Case B10*, *Case B20*, and *Case B30*. (b, f, j) The second column presents the time-averaged and azimuthally averaged angular velocity with radius and latitude, with the fast prograde equator in red and slower poles in blue. (c, g, k) Azimuthally averaged and time-averaged temperature fluctuations (where the  $\ell = 0$  component has been removed) with the warm poles in red tones and the cool equator in blue tones. (d, h, l) The stream function of the meridional flow ( $\psi$ ), clockwise (CW) flows in red, and counterclockwise (CCW) flows in blue. The dashed line in the second, third, and fourth columns delineates the beginning of the stable region.

(A color version of this figure is available in the online journal.)

global overturning time, which is between 15 and 30 days for these  $1.2 M_{\odot}$  simulations. These convective structures are very similar to the linearly unstable columnar modes arising in the presence of a significant density gradient and a convex boundary (Busse 2002; Jones et al. 2009). The convective columns form a thermal Rossby wave that has a phase velocity larger than the local rotation rate, leading to downflows that propagate prograde faster than the local differential rotation. In a linear regime, the effects of compressibility counteract the tendency of the convection to occur along the tangent cylinder, where it instead increasingly occupies the outermost portions of the domain (Jones et al. 2009). In our simulations, however, these effects often lead to two sets of columnar structures, one being

somewhat more confined to larger radii and another that occurs deeper along the tangent cylinder. The primary difference in the simulations here is that they are highly supercritical with a realistic stratification, yet these structures largely persist despite their nonlinear interaction with turbulent flows.

The downflow sheaths surrounding the upflows are elongated in azimuth, forming thin sheets that spiral outward from the base of the convection zone in a prograde direction. Such structures are largely due to vortex stretching near the upper boundary that is enhanced by the effects of compressibility, both of which are in turn due to our choice of a Prandtl number that is less than unity (Zhang 1992; Jones et al. 2009). This prograde spiraling leads to strong Reynolds stresses that act in concert with the thermal

state to help build the strong zonal flow and thus the differential rotation seen in these simulations (see Sections 6.2 and 7). The radial differential rotation, as seen in panels (b), (f), and (j) of Figure 3, which increases with larger rotation rates, also must play a role in stretching out these columns. The latitudinal differential rotation tends to shear the columns, creating the so-called banana cells. There also tends to be less latitudinal connectivity in the downflow networks than in more slowly rotating cases. This enhanced connectivity at lower angular velocities can prevent the formation of the columnar structures so prevalent in cases with a larger angular velocity.

The number of such convective modes that can fit within the circumference of the star increases with rotation rate and thus the Taylor number (Gilman & Glatzmaier 1981; Dormy et al. 2004; Jones et al. 2009). This means that at a given radius these modes will have less longitudinal extent as exhibited in panels (a), (e), and (i) of Figure 3. Analyses carried out using the modal equations of rotating Boussinesq convection within tangent cylinders (Dormy et al. 2004) and numerical computations of linear modes in compressible anelastic convection (Gilman & Glatzmaier 1981; Jones et al. 2009) reveal that the azimuthal wavenumber of the most unstable mode increases as  $m = m_c \text{Ta}^{1/6}$ , where  $m_c$  is the critical wavenumber. For our cases, the viscosity scales as  $\Omega_0^{-2/3}$ ; thus, the most unstable mode is only a function of the rotation rate, where  $m = m_c (\Omega_0/\Omega_\odot)^{5/9}$ . The critical mode is determined by using a value estimated from those given in Jones et al. (2009) as  $\hat{m}_c$  and the values of convection zone depth, viscosity in *Case A5*, and its rotation rate in the Taylor number, which yield  $m_c \approx 2^{1/3} 5^{-2/9} \hat{m}_c d^{2/3} \nu_{A5}^{-1/3} \Omega_\odot^{1/3} = 9$ . The resulting wavenumbers agree well with the modes that are most visible at the equator in cases *Case A5*, *Case A10*, and *Case A20* that have azimuthal order of  $m = 22, 32$ , and  $54$ , whereas the brief analysis here yields  $m = 22, 32$ , and  $47$ . There is likely a discrepancy between the order of the two modes for the fastest rotators because an instability arises in these cases that may change this scaling (see Section 3.5).

At higher latitudes inside of the tangent cylinder, the convection is more isotropic and the downflow networks organize on scales smaller than in the equatorial regions, as is seen in panels (a), (e), and (i) of Figure 3. These convective cells are intricate and dynamic, with cells constantly evolving as they interact with one another and the bulk motions. When viewed on a spherical shell, the downflows of the high-latitude convective cells take on a crescent-like shape and precede the upflows as both are carried along by the differential rotation. As described by the Taylor–Proudman theorem, the tendency for these flows to align with the rotation axis becomes more pronounced at higher rotation rates. Indeed, as the angular velocity of the frame increases, the high-latitude downflows form into cylindrical sheaths nearly aligned with the rotation axis. Such convective structures have a strong vertical vorticity. The sense of this vorticity in the downflow plumes is cyclonic above the middle of the convection zone: counterclockwise (CCW) in the northern hemisphere and clockwise in the southern. As the plumes descend deeper into the convection zone, their vorticity changes sign, and the downflows become anti-cyclonic (Miesch et al. 2000, 2008). The upflows, on the other hand, are anti-cyclonic at all depths outside the tangent cylinder and at latitudes above about  $\pm 60^\circ$ . However, at mid-latitudes the upflows are anti-cyclonic in the upper convection zone but are cyclonic in the lower portion.

In Table 2, flow diagnostics for the last two  $1.2 M_\odot$  F-type star simulations (*Case A5i* and *Case A20i*) are shown. The

computational domain of these two simulations is restricted in radius to be only in the convectively unstable portion of the domains of the other  $1.2 M_\odot$  F-type star simulations. Placing the lower boundary of the domain at the bottom of the convection zone is tantamount to having an infinitely stiff entropy gradient there, eliminating penetrative motions. While the convective patterns are largely unchanged in these simulations, the rate of deceleration of downflow plumes generally increases as they approach the lower boundary. This alters the Reynolds stress correlations and turbulent enthalpy flux, which in turn changes the differential rotation, meridional circulation, and temperature structures established in these simulations and will be discussed further in Section 5.

### 3.2. Case B: $1.3 M_\odot$ Simulations

Three  $1.3 M_\odot$  F-type star simulations are shown in Figure 4, *Case B10*, *Case B20*, and *Case B30*. The two *Case B* simulations carried out at 10 and 20 times the solar rate allow for an easy comparison to the two *Case A* simulations at the same rotation rate. The third simulation (*Case B30*) exhibits modulated convection that is not seen in the other cases and therefore is shown for its inherent interest. A striking similarity is seen between the convective patterns established in the *Case B* simulations and the *Case A* simulations (Figures 4(a), (e), and (i)). There is still a transition from columnar convection outside the tangent cylinder to more isotropic and smaller scale convective cells inside of it. For these simulations, the edges of the tangent cylinder intersect the upper boundary at latitudes of  $\pm 26^\circ, 6^\circ$  closer to the equator than in the  $1.2 M_\odot$  F-type stars.

Careful scrutiny reveals that the columnar equatorial convective modes, as seen in the Mollweide projections of the radial velocity (Figures 4(a), (e), and (i)), have less of a latitudinal extent when compared to the  $1.2 M_\odot$  simulations. The radial velocities are about 15% larger on average than in the *Case A* series of simulations, but the tails of the radial velocity distribution extend out even further to several  $\text{km s}^{-1}$  in the downflows. The difference in temperature fluctuations between the center of an upflow and the downflows at its edges is about 120 K, 50% larger than in the  $1.2 M_\odot$  F-type stars. These somewhat larger velocities and temperature fluctuations are expected given that both the lower background density is lower and the luminosity is 50% higher in the  $1.3 M_\odot$  simulations. As seen in Table 2, there is a single case that captures only the convectively unstable region, *Case B20i*. This case is meant to be a point of comparison for assessing the role of overshooting in maintaining a strong differential rotation.

The mean angular velocities and temperature variations for *Case B10*, *Case B20*, and *Case B30* are shown in the second and third columns of Figure 4. The nine panels in the last three columns of Figure 4 all demonstrate the convection zone geometry of the *Case B* simulations. The convection zone is much narrower than in both the Sun and the  $1.2 M_\odot$  F-type stars. This narrowing of the convectively unstable region and the increased luminosity of the higher mass stars play a role in the behavior of the differential rotation established in these simulations.

### 3.3. Average Flows

Shown in the second column of Figure 3 are the mean radial and latitudinal profiles of angular velocity ( $\Omega = \Omega(r, \theta)$ ) achieved in *Case A5*, *Case A10*, and *Case A20*. These profiles are averaged in longitude and in time, over 150 days. All of the

1.2  $M_{\odot}$  F-type star simulations exhibit solar-like differential rotation profiles, with prograde (fast) equators and retrograde (slow) poles. Contours of constant angular velocity, black lines in Figures 3(b), (f), and (j), are largely radial but become increasingly aligned with the rotation axis with more rapid rotation.

More specifically, the average rotation profile in depth and latitude established in *Case A10* are shown in Figure 3(f). The red and white tones indicate a fast prograde equator, while the black and blue tones indicate a pole rotating more slowly than the frame rate; this is considered solar-like differential rotation. The color associated with the frame rate of 4240 nHz is yellow. The rotational shear averaged over the convection zone between the equator and the pole is  $\Delta\Omega = 1290$  nHz, corresponding to a relative latitudinal shear of  $\Delta\Omega/\Omega_0 = 34\%$ . Thus, this simulation has a latitudinal shear that is quite similar to that observed at the solar surface. Similarly, *Case A5* and *Case A20* possess an equator-to-pole absolute differential rotation of  $\Delta\Omega = 560$  nHz or  $\Delta\Omega/\Omega_0 = 26\%$  and  $\Delta\Omega = 2330$  nHz or  $\Delta\Omega/\Omega_0 = 27\%$ . Though we have attempted to drop the diffusion within the stable region, we are restricted in both the depth of the layer and the magnitude of the motions that still require some diffusion. This leads to a slow spread of the differential rotation into the stable region, which can be seen in Figures 3(b), (f), and (j).

A trend is readily discernible; the absolute contrast of angular velocity grows in latitude and radius with more rapid rotation. These profiles show some weak asymmetry between the northern and southern hemispheres, but only at lower rotation rates and at high latitudes. This behavior would likely disappear if very long time averages were taken. Variation between the hemispheres should be expected as the patterns of convection, and thus the mean zonal flows, are not symmetric about the equator.

The streamlines of the time-averaged meridional mass flux ( $\psi$ ) are shown in the last column of Figure 3. The stream function  $\psi$  is defined such that  $\langle \rho \mathbf{u}_m \rangle = \nabla \times \psi \hat{\phi}$ . The sense of the flow is CCW for the blue contours and clockwise (CW) for the red. There is typically a CCW cell of meridional flow in the northern hemisphere, and a CW cell in the southern hemisphere, that stretches from the inner edge of the tangent cylinder to the pole, indicating a poleward meridional flow in the upper convection zone and an equatorward flow near the base of the convection zone. These high-latitude cells are very large scale flows and are thus constrained by the global spherical geometry. These flows reside mostly on contours of constant radius and possess weaker meridional flows than the low-latitude cells. Outside the tangent cylinder the mean meridional flow is dominated by the columnar structures seen in the Mollweide projections of the radial velocity in Figures 3(a), (e), and (i).

The meridional flows associated with these structures have streamlines that are quite complicated, having multiple cells in radius and latitude. The trend is that the number of cells increases with rotation rate, primarily with more cells in radius. These cells are aligned with the rotation axis and extend from the upper radial boundary to the equator where they close, indicating that there is very little mean cross-equatorial flow or flow across the tangent cylinder. The net effect of these low-latitude cells is to largely isolate the equatorial region from higher latitudes inside the tangent cylinder. This behavior can be understood by considering the latitudinal connectivity of the downflow networks established in the convection; at low rotation rates there is a tendency for a large degree of latitudinal connectivity

that is reduced at higher rotation rates due to the influence of the Coriolis forces. The meridional circulations established within the *Case B* simulations are similar in morphology to those in the *Case A* simulations. They are multi-cellular at low latitudes and single celled at high latitudes, as seen in the streamlines of the meridional flow ( $\psi$ ) shown in Figures 4(d), (h), and (l).

### 3.4. Average Temperature Fluctuations

The azimuthally averaged and time-averaged profiles of temperature fluctuations about the spherical mean are shown for *Case A5*, *Case A10*, and *Case A20* (Figures 3(c), (g), and (k)). A clear pattern arises in these simulations, where the poles are warm and the equator is cool, while mid-latitudes are cooler yet, relative to the background temperature. These fluctuations are nearly constant on cylinders, especially at high latitudes. Such a pattern has also been found in simulations of global-scale convection in G-type stars (Brown et al. 2008). The origins of these fluctuations are discussed in detail in Section 6.

These fluctuations about the spherical mean are generally still small but become more significant for more rapid rotation rates. In *Case A20*, for instance, the temperature fluctuations near the top of the simulation are about 3% of the background value, or about 3000 K. All of the cases presented here have similar latitudinal profiles in temperature. The latitudinal temperature contrast between the equator and 60° latitude increases markedly at higher rotation rates as shown in Table 3. Indeed, the primary difference between the *Case B* simulations and those shown for the *Case A* simulations is that the absolute latitudinal contrasts of differential rotation and temperature fluctuations are larger (see Section 8), but the structure is largely the same with slow, warm poles and a cool, fast equator (Figures 4(c), (g), and (k)).

### 3.5. Modulated Convection and Shear Instabilities

Spatially modulated convection, such as that discussed in Brown et al. (2008), becomes readily apparent in *Case B30* (Figure 4(i)). The convection in the equatorial region is less vigorous at certain longitudes and more so at others. In this simulation, there is a roughly  $m = 1$  modulation in the equatorial convection. This modulation is increasingly pronounced with depth and is most evident in the stable region where the overshooting convection and gravity waves are confined to a horizontal region covering roughly a quarter of the sphere at the equator and converging at the poles. This localized overshooting convection feeds back onto the upflows initiated at the base of the convection, giving them a substantially larger temperature perturbation than elsewhere on the sphere generating faster flows. This case is also slightly off the path in parameter space followed in the other cases in that the diffusivity is the same as in *Case B20* and thus is about 25% higher than expected given its bulk rotation rate. This is to avoid the high cost of increasing the resolution of the simulation and the subsequently longer evolution time.

The presence of a sufficiently large differential rotation within a convectively stable region can give rise to a global shear instability similar to Rossby–Haurwitz or planetary waves (Haurwitz 1940; Longuet-Higgins 1964; Kitchatinov 2010). These waves can efficiently transport energy and angular momentum between the equatorial region and the poles. Such an instability has arisen in the radiative zone of *Case A15*, *Case A20*, and *Case B20*, where several low-degree spherical harmonic modes are unstable as are visible for *Case B20* in Figure 5. These motions have a pressure and vorticity signature that prints through the convection zone, surviving despite the vigorous convection

**Table 3**  
Global Properties of the Evolved Convection

Mass	Case	KE/10 <sup>6</sup>	KE <sub>DR</sub> /10 <sup>6</sup>	KE <sub>MC</sub> /10 <sup>3</sup>	KE <sub>C</sub> /10 <sup>6</sup>	$\Delta\Omega_r/\Omega_0$	$\Delta\Omega_{60}/\Omega_0$	$\Delta T_{60}$	$\Delta S_{60}$	$d_0/H_P$
1.2 $M_\odot$	A5	7.46	6.35 (85.1%)	5.39 (0.072%)	1.10 (14.8%)	0.065	0.195	-117	-20750	0.088
	A7	15.0	13.9 (92.9%)	4.31 (0.029%)	1.07 (7.11%)	0.063	0.212	-246	-44830	0.089
	A10	29.4	28.4 (96.6%)	3.68 (0.013%)	1.01 (3.42%)	0.054	0.211	-501	-93010	0.101
	A15	67.1	65.3 (97.4%)	2.44 (0.004%)	1.74 (2.60%)	0.043	0.200	-1048	-184400	0.339
	A20	91.9	90.4 (98.4%)	1.99 (0.002%)	1.51 (1.65%)	0.037	0.177	-1635	-290300	0.332
	A5i	6.92	5.65 (81.7%)	6.04 (0.087%)	1.26 (18.2%)	0.057	0.199	-101	-13900	...
	A20i	28.5	27.5 (96.5%)	2.48 (0.009%)	0.99 (3.47%)	0.049	0.114	-714	-44940	...
1.3 $M_\odot$	B8	2.23	1.41 (63.1%)	2.93 (0.131%)	0.82 (36.8%)	0.030	0.101	-190	-31000	0.121
	B10	6.70	5.99 (89.3%)	2.46 (0.037%)	0.71 (10.7%)	0.038	0.177	-613	-111670	0.122
	B15	15.5	14.6 (94.4%)	1.97 (0.013%)	0.86 (5.55%)	0.041	0.204	-1444	-267900	0.137
	B20	35.0	33.8 (96.5%)	1.53 (0.004%)	1.22 (3.49%)	0.036	0.224	-2799	-503200	0.334
	B30	26.4	25.6 (97.2%)	0.88 (0.003%)	0.75 (2.83%)	0.024	0.142	-3745	-812000	0.358
	B20i	15.3	14.6 (95.5%)	1.43 (0.009%)	0.69 (4.51%)	0.038	0.182	-1797	-224100	...

**Notes.** Total (KE), differential rotation (KE<sub>DR</sub>), meridional circulation (KE<sub>MC</sub>), and convective (KE<sub>C</sub>) kinetic energy densities are both averaged in time and volume and are shown in units of erg cm<sup>-3</sup>, and relative to the total kinetic energy in parentheses. The spatial averages are taken only over the convection zone to allow comparison between the cases with and without overshooting. The relative radial and latitudinal differential rotation ( $\Delta\Omega_r/\Omega_0$  and  $\Delta\Omega_{60}/\Omega_0$ ), the latitudinal temperature difference ( $\Delta T_{60}$ , in K), and the latitudinal entropy difference ( $\Delta S_{60}$ , in erg K<sup>-1</sup> cm<sup>-3</sup>) are measured between the equator and 60° latitude (averaged over both hemispheres). The depth of the overshooting region ( $d_0$ ) is shown measured relative to the pressure scale height ( $H_P$ ) at the base of the convection zone and is horizontally averaged.

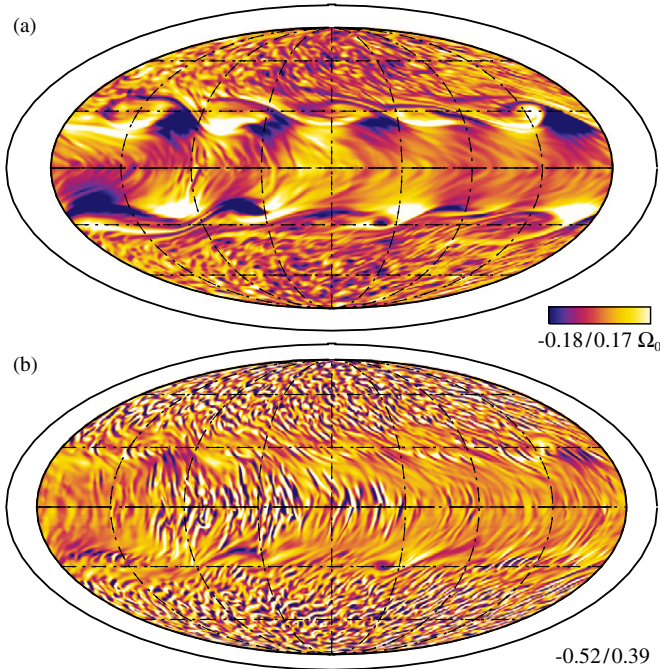


**Figure 5.** Large-scale shear instability existing within the stable region prints through the convection zone as evident in *Case B20*. Mollweide projections of the radial vorticity ( $\omega_r$ ) are shown relative to the vorticity of the reference frame ( $\Omega_0$ ) and at two depths with the  $m = 0$  component removed (a) 0.86  $R$  and (b) 0.92  $R$ . Dark tones indicate negative radial vorticity.

(A color version of this figure is available in the online journal.)

present there as in Figure 5(b). The instability of these modes is sensitive to the magnitude of the differential rotation and to its latitudinal profile (Watson 1981; Kitchatinov 2010). Furthermore, it has significant impact on the overshooting convection, allowing mixing to greater depths (Figure 8(c)). We will present the details of these solutions and an analysis of them in a forthcoming paper (K. C. Augustson et al. 2012, in preparation).

#### 4. EXAMINING DYNAMICS WITHIN CASE A10

The convective patterns, like those discussed in Section 3.1, are complex and time dependent with asymmetries between

upflows and downflows due to mass conservation in a stratified medium. The downflows are cold, fast, and narrow and border their more leisurely ascending counterparts. The convective cells are outlined by the dark downflows visible in the radial velocities shown in the top four panels of Figure 6.

##### 4.1. Typical Flows and Thermal Properties

The archetypal convective cell is defined by a central broad upflow bordered by narrow downflows. Indeed, the color tones in Figures 6(a)–(d) are meant to construe both the sign of the temperature fluctuations (Figures 6(e)–(h)) associated with these structures and the direction of the flow. Namely, the upflows are warm and the downflows are cool relative to the mean temperature. Radial velocities that are within  $1\sigma$  of the mean at mid-convection zone for the flows in *Case A10* are between  $-230$  m s<sup>-1</sup> for downflows and  $190$  m s<sup>-1</sup> for upflows, where the rms radial velocities are  $150$  m s<sup>-1</sup>. Large- and small-scale thermal structures are visible in Figures 6(e)–(h), where the large  $m = 0$  temperature perturbations have been removed. The average difference of temperature fluctuations between the central upflow and the bordering downflows defining the convective cell is about 45 K at mid-convection zone and increases with height. A large-scale structure corresponding to an  $m = 1$  spherical harmonic mode is also visible. This global-scale pattern persists for long periods of time and is most evident in the more rapidly rotating cases.

The effects of the stratification are visible in the patterns of the convection in Figures 6(a)–(c). The convective cells near the surface in panel (a) show the greatest asymmetry in areal coverage and rms radial velocity between the upflows and the downflows. This asymmetry is reduced at greater depths as in panel (c) as the upflows and downflows become increasingly symmetrized both in the rms velocities achieved and in areal extent due to the larger local density scale height. The temperature field appears slightly more diffuse than the radial velocity due to the thermal diffusion being four times greater, as reflected in the Prandtl number being 1/4 at all depths. However, it shows the changes in the morphology of the convection that are similar to those of the radial velocity, where the longitudinal extent and magnitude of the temperature fluctuations of the convective cells decrease with depth.

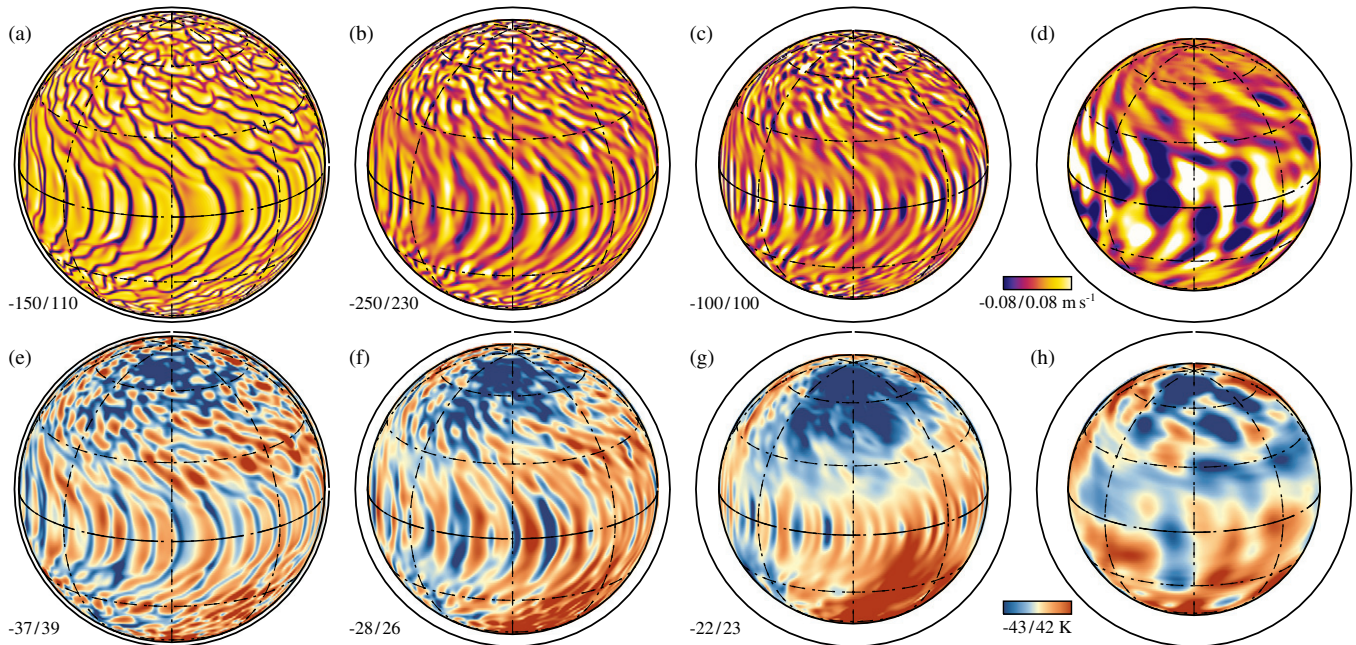


**Figure 6.** Radial velocities ( $u_r$ ) and temperature fluctuations ( $T'$ ) at several depths in *Case A10*. The temperature fluctuations are taken about the  $m = 0$  component, removing the largest scale variations. The quantities  $u_r$  and  $T'$  are shown in orthographic projection at several radial levels with  $r/R$  equal to (a, e) 0.97, (b, f) 0.92, (c, g) 0.85, and (d, h) 0.80. Light tones are warm upflows, while dark tones are cool downflows. Panels (d) and (h) show flows within the radiative zone. (A color version of this figure is available in the online journal.)

The areal filling factors of the upflows and downflows are roughly  $2/3$  and  $1/3$ , respectively, when averaged over the convection zone. There is a further asymmetry in the magnitudes of the radial velocity within these flows, with the downflows being faster than the upflows. Indeed, the distribution of the radial velocities has a large negative skewness within the convection zone. The distribution of radial velocities in the downflows has a tail that is about twice as long as the distribution of velocities in the upflows. These properties are similar to the flows established in solar simulations detailed in Miesch et al. (2008). Further, the mean negative radial velocity is about twice as large as the mean positive radial velocity. This asymmetry in the radial velocities reflects the density stratification and mass conservation, with the caveat that the degree of asymmetry is dependent on the level of turbulence within a simulation where higher Reynolds numbers lead to more asymmetry.

The downflows, visible as dark lanes in Figures 6(a)–(c), are initiated by cooling near the surface and sustained through buoyancy driving within the bulk of the convection zone. The cooler and more dense downflows entrain fluid from the surrounding upflows through mass conservation and diffusion. These processes act to erode the density contrast between the downflow and the surrounding fluid. Thus, the downflows experience less buoyancy driving as they fall deeper into the convection zone. Even without a significant buoyancy to provide a downward acceleration, they have enough momentum to continue under their own inertia. Once the downflows reach the bottom of the convection zone, they become buoyantly braked as they enter the stable region. However, they continue into the uppermost reaches of the radiative zone through their own inertia, as in Figures 6(d) and (h). Eventually they are fully braked, but not before they have penetrated a significant distance into the stable region. Such overshooting motions can excite gravito-inertial waves that propagate within the stable region. These waves are eventually dissipated through diffusive

processes but can play a role in the redistribution angular momentum and energy (Rogers & Glatzmaier 2006; Brun et al. 2011).

#### 4.2. Energetics of the Convection

These flows give rise to the transport of energy and momentum throughout the domain. The energy transport by resolved convective motions will not in general be equivalent to the mixing-length prescriptions assumed in the 1D solar structure model, so the simulation must adjust accordingly. In a steady state, an equilibrium is reached that balances the different components of the mean radial transport of energy.

The large outward enthalpy flux  $L_{\text{en}}$  seen in Figure 7(a) exceeds the luminosity of the star at its peak and is balanced primarily by the unresolved eddy flux  $L_{\text{ed}}$  near the top of the domain and by the radiative flux  $L_{\text{rd}}$  below mid-convection zone to produce a nearly constant stellar luminosity throughout the domain. While the upflows contribute about 10% of the enthalpy flux, the dominant factors contributing to the enthalpy flux are the downflows. These flows are cool relative to the mean value as seen in the temperature fluctuations of Figure 6; this correlation between the negative fluctuating temperature and the negative radial velocities leads to a radially outward enthalpy flux. There is significant latitudinal variation in the enthalpy flux, with the largest positive flux in the polar regions and with fluxes that are about 30% less outside of the tangent cylinder. Near the base of the convection zone, indicated by the dashed line in Figure 7, the enthalpy flux becomes negative due to the overshooting convection, as will be discussed in the following section. The overshooting enthalpy flux attains its most negative value near the poles, though when integrated over the stable and overshooting regions it peaks at the tangent cylinder. This variation in the enthalpy flux reflects the latitudinal variation in the depth of the overshooting.

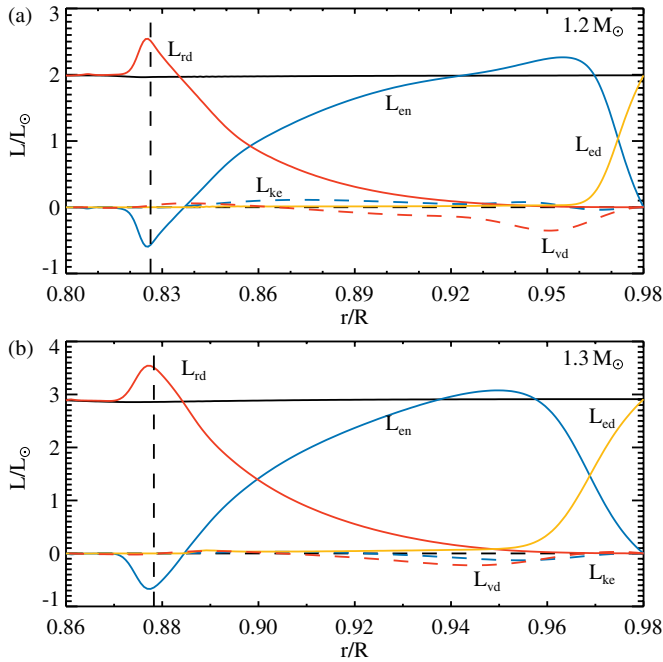


**Figure 7.** Time- and horizontally averaged radial energy fluxes for (a) *Case A10* and (b) *Case B10*. Fluxes are shown as luminosities ( $L = 4\pi r^2 F$ ) and taken relative to the solar luminosity with the total ( $L_{\text{tot}}$ ) shown as a solid black line. The components of the total flux are the kinetic energy flux ( $L_{\text{ke}}$ , dashed blue), enthalpy flux ( $L_{\text{en}}$ , solid blue), radiative flux ( $L_{\text{rd}}$ , solid red), unresolved eddy flux ( $L_{\text{ed}}$ , solid orange), and viscous diffusive flux ( $L_{\text{vd}}$ , dashed red). The vertical dashed line indicates the radius at which the mean entropy gradient changes sign.

(A color version of this figure is available in the online journal.)

The asymmetrically larger velocities in the downflows give rise to an inward kinetic energy  $L_{\text{ke}}$  (inside the tangent cylinder) that is due to the cubic dependence on the velocity. Outside the tangent cylinder, the columnar equatorial flows produce a net outward kinetic energy flux, dominated by the large zonal velocity component, that are on average slightly larger than the higher latitude components and lead to a small net outward flux for *Case A10* (Figure 7(a)).

## 5. CONVECTIVE OVERSHOOTING

The Péclet number ( $\text{Pe} = \text{Re}/\text{Pr}$ ) of the radial flows is of essential importance in determining the properties of the overshooting convection (e.g., Brummell et al. 2002; Brun et al. 2011). Small values of  $\text{Pe}$  give rise to convective overshoot, in the sense that the stratification remains sub-adiabatic. Large  $\text{Pe}$  values, those much greater than one, promote efficient entropy mixing such that the stratification becomes nearly adiabatic, and the base of the convection zone can spread downward in time if nothing acts to oppose the spreading. In the stable region, the Péclet number is about  $1/40$  at the lower boundary, around 1 in the overshooting region, and approximately 10 in the bulk of the convection zone. Therefore, it is expected that the motions at the base of the convection zone are overshooting rather than penetrative. This is indeed the case, as demonstrated in Figure 2(a), where the evolved mean entropy gradient is shown for *Case A10* and *Case B10*. However, all the cases reported on here possess a strongly sub-adiabatic region below the convection zone that is essentially fixed in time. It extends from the lower boundary to the radius at which the entropy gradient changes sign or the bottom of the convection zone. The

mixing there is inefficient and the stratification remains largely unchanged as indicated by the Péclet number there (Zahn 1991; Spiegel & Zahn 1992; Brummell et al. 2002). The width of this layer is likely overestimated because this width scales as the square root of the filling factor of the downflowing plumes, which are likely larger in these simulations than in the actual stars (Zahn 1991; Rempel 2004).

In the region of overshooting, on the other hand, the entropy gradient is steepened significantly compared to the stellar model. This is a consequence of the downflows within the convection dragging cool fluid to the bottom of the domain, where they are then quickly heated due to buoyancy braking in the region of overshooting as will be seen in the following section. While there is not a physical boundary at the bottom of the convection zone, the rapid increase in the entropy gradient acts very much like a wall that rapidly slows downflows. However, these flows overshoot into the stable region where the work done by buoyancy rapidly brakes and heats them. This allows the fluid to thermally equilibrate with the surrounding fluid. The stronger downflows, those that are cooler and faster than the majority in the convection zone, retain enough inertia to flow past the bottom of the convection zone and continue to be buoyantly heated. They quickly become warmer than the surrounding fluid but are still traveling into the stable region. Thus, correlations between the fluctuating temperature and the radial velocity in the overshooting convection give rise to a substantial negative enthalpy flux as seen in Figure 7, where it reaches around half of a solar luminosity. This is in contrast to 1D stellar structure models, where there is either a small, negative overshooting enthalpy flux or none depending on how the overshooting is parameterized.

In Figure 8, we quantify the beginning of the overshooting region by the radius  $r_c$  where the enthalpy flux becomes negative, the radius at which the entropy gradient equals zero ( $r_{\text{bcz}}$ ) is demarked by the dashed line, and the bottom of the overshooting region occurs at a radius where the negative enthalpy flux of the overshooting convection equals 1% of the most negative value ( $r_o$ ). It is clear from Figure 8(a) that the convection zone in *Case A10* is most shallow around  $\pm 20^\circ$  (at about 3% of the stellar radius  $R$ ) and is deepest at the equator ( $0.0075 R$ ), with an average width of  $0.015 R$ . The overshooting region in *Case B10* is 1.5% of the stellar radius at its deepest around  $\pm 20^\circ$ ,  $0.009 R$  at its most shallow at the equator, and  $0.0125 R$  on average. The depth of overshooting at the equator is reduced as the centroid of the region of the overshooting occurs at a greater depth due to the penetration of the convection, resulting in convection that feels a much stiffer stratification. At higher latitudes, the centroid of the overshooting region occurs at a larger radius, which results in a larger region of overshooting as the convection feels a less stiff stratification.

The bottom of the overshooting region is deepest at low latitudes and most shallow at the poles in *Case A10*, which implies that the radiative zone is slightly prolate. In *Case B10*, the bottom of the overshooting region is essentially spherically symmetric. This is also true of the radius of the base of the convection zone ( $r_{\text{bcz}}$ ), which has almost no latitudinal variation in both cases. The radius at which the enthalpy flux becomes negative ( $r_c$ ) is everywhere larger than  $r_{\text{bcz}}$ . This property arises from some of the downflow plumes having a change in the sign of their fluctuating temperature (from cool to warm) that precedes their arrival at  $r_{\text{bcz}}$ . The downflows are diffusively heated by the warm upflows that surround them, which occurs because the time for the downflow to cross the distance between

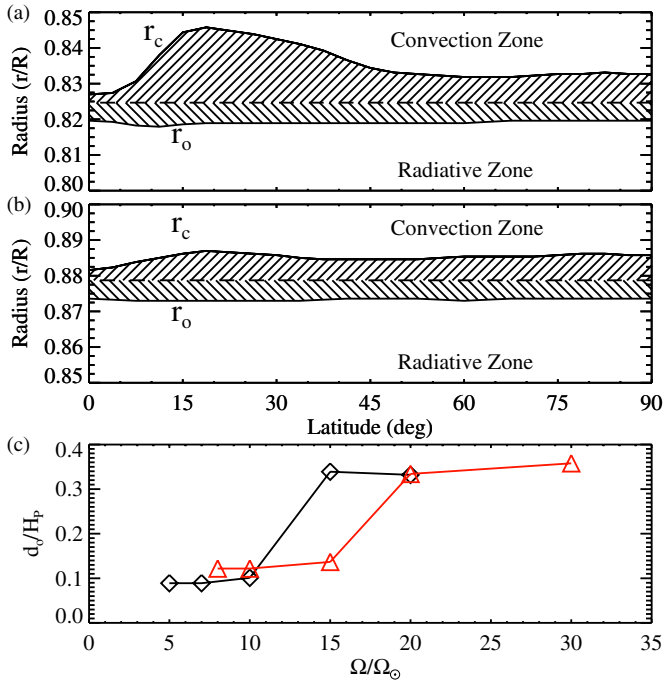


**Figure 8.** Changes in the radial extent of overshooting motions with latitude. Shown as a shaded region below  $r_{\text{bcz}}$  for (a) *Case A10* and (b) *Case B10*. The radii where the enthalpy flux is negative encompass the full shaded region. The radius at which there is a transition to the convection zone is denoted by  $r_c$ . The lower boundary of the overshooting motions is denoted by  $r_o$ . The scaling with rotation rate of the depth of the overshooting region relative to the pressure scale height at  $r_{\text{bcz}}$  is ( $d_o/H_p$ ) for cases A and B.

(A color version of this figure is available in the online journal.)

$r_c$  and  $r_{\text{bcz}}$  is longer than the horizontal diffusion time across the downflow. This results in a negative enthalpy flux that begins before the bottom of the convection zone and builds to its most negative values as the downflows continue into the stable region where they are buoyantly heated.

We have conducted simulations with the same initial stellar model, but without the region of penetration, these are *Case A5i*, *Case A20i*, and *Case B20i*. It is clear from Table 3 that these simulations have much weaker latitudinal entropy and temperature contrasts than their counterparts with a stable region. However, the equator to  $60^\circ$  differential rotation contrast is only slightly lower. Hence, the inclusion of a stable region alters several aspects of the mean thermal state and flows, where it primarily leads to a tilting of the contours of the angular velocity toward being conical. It also leads to a stronger scaling of the latitudinal temperature gradient with rotation rate. The primary driver behind this is that there is an enhanced equatorward latitudinal enthalpy flux relative to the cases that have a stable region. The meridional circulation kinetic energy, on the other hand, is lower in cases with a region of overshooting than those without. This behavior arises due to a change in the axial torque near the lower boundary. The impenetrable lower boundary imposes a much stronger constraint on the flows; indeed, all flows must halt at this point. This means that the divergence of both the Reynolds and the viscous stresses must be larger in simulations with an impenetrable boundary when compared to simulations with a region of overshooting, as is indeed the situation in *Case A5i*, *Case A20i*, and *Case B20i*. The equation of gyroscopic pumping (cf. Section 7 and Equation (20)) implies that this leads to a larger meridional

circulation kinetic energy as is evident in the energies given in Table 3.

## 6. THERMAL STRUCTURING

As an example of the mean thermal structure established in these simulated stars, consider the time-averaged and azimuthally averaged temperature fluctuations for *Case A10* (Figure 9(a)). It is clear that the perturbations do not have a zero mean, as expected from the broken spherical symmetry arising from the rotation of the system. The temperatures range from the hot poles at 840 K to the cool equator at  $-280$  K with yet cooler mid-latitudes. This equator-to-pole temperature contrast is slightly more than two orders of magnitude greater than the observational limits on the latitudinal temperature profile of the Sun (Rast et al. 2008). However, these variations are taken relative to the mean temperature that varies between  $1.3 \times 10^6$  K at the bottom of the domain and  $10^5$  K at the top, so they are still relatively small, being of order 1%. These averaged temperature fluctuations are nearly constant on cylinders at latitudes above  $\pm 45^\circ$ , while it has a positive radial gradient at lower latitudes. This distribution of temperature fluctuations impacts the local energy flux balance and is intimately linked to the differential rotation and meridional flows, such as those seen for *Case A10* in Figures 3(f) and (h).

### 6.1. Principal Contributions to Temperature

The time-averaged and azimuthally averaged temperature fluctuations are decomposed into the fluctuating pressure and entropy components ( $T = P/\bar{\rho}c_p + \bar{T}S/c_p$ ), from which it becomes apparent that the pressure is the largest contributor (Figures 9(b) and (c)). This is especially true at latitudes above  $45^\circ$ , where the pressure perturbation has nearly radial contours and contains about 80% of the amplitude of the temperature fluctuations. At these higher latitudes, the entropy contribution tilts the contours of the temperature fluctuations to be nearly cylindrical. At low latitudes, the two components play more equal roles, at least within the deep convection zone. Figure 9(d) exhibits the latitudinal structure of the mean temperature fluctuations at several depths: near the top of the domain, at mid-convection zone, and in the stable region. There is a substantial change in the temperature structure with depth outside the tangent cylinder where it swings from  $-280$  K in the stable region to almost 0 K near the top of the domain at the equator. The entropy and pressure act in tandem to depress its value at the base of the convection zone and the pressure drives its value above zero near the surface where the entropy contribution wanes. Figure 9(e) shows the mean entropy fluctuations at the same depths as in panel (d). The entropy fluctuations increase nearly monotonically in latitude and have little radial variation. This mean latitudinal entropy structure arises due to a balance of energy fluxes in latitude. As the simulation evolves and reaches a steady state, the turbulent enthalpy flux and kinetic energy flux adjust to achieve a balance with the diffusive flux of entropy in latitude. Once in this statistically steady state, the mean latitudinal energy fluxes do indeed balance and thus lead to the mean latitudinal structures seen in Figures 9(c) and (e).

In *Case A10*, the background temperature decreases by about a factor of 10 across the convection zone, and since it weights the entropy fluctuations, it causes an equivalent decrease in them (Figure 9(c)). The decrease is in part due to the weak radial differential rotation in *Case A10* (Figure 3(f)). Indeed,

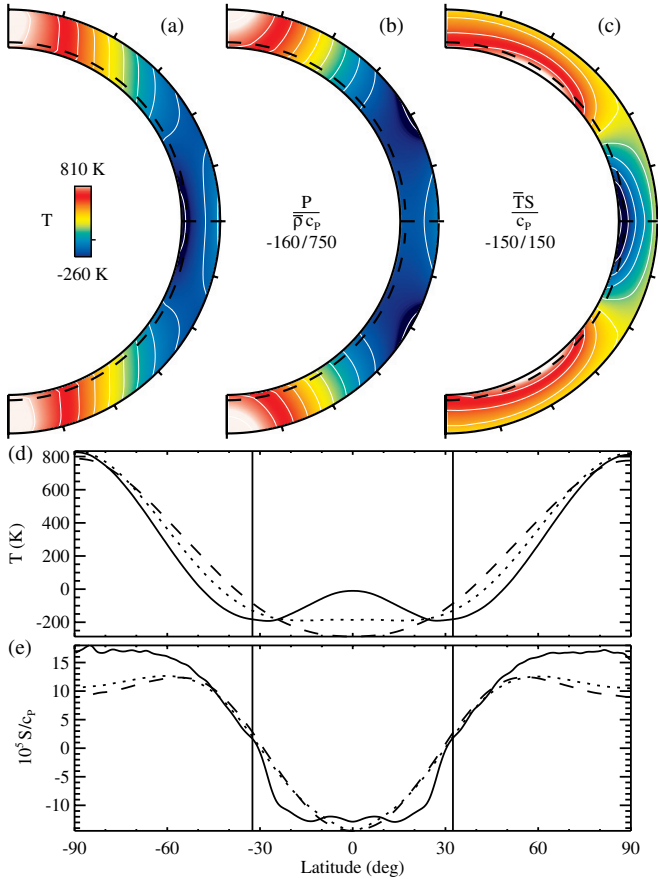


**Figure 9.** Fluctuating thermal structures found within *Case A10*. Azimuthally averaged variations are shown for (a) the temperature and the scaled contributions from the fluctuations of (b) pressure  $[P/\bar{\rho}c_p]$  and (c) entropy  $[TS/c_p]$ . Cuts through (d) the averaged temperature fluctuations and (e) the averaged entropy fluctuations are displayed at fixed radii: at the top of the domain (solid line,  $0.98 R$ ), at mid-convection zone (dotted line,  $0.89 R$ ), and in the stable region (dashed line,  $0.80 R$ ). The vertical lines denote the edges of the tangent cylinder.

(A color version of this figure is available in the online journal.)

a time-steady meridional force balance leads to a linking of the entropy to the ageostrophic component of the differential rotation (see Section 6.2), which implies that a strong radial differential rotation could lead to a larger entropy contribution. But as is evident in Figure 9(e), the entropy perturbations have little variation in radius, reflecting the weak radial differential rotation. In an azimuthal and time average of the momentum equation (Equation (1)), the time and azimuthal derivatives of the mean flows vanish, leaving the advection, viscous, Coriolis, buoyancy, and pressure gradient terms. If we keep only the largest contributing terms, the gradient of the zonally averaged pressure fluctuations is then primarily balanced by three terms: the buoyancy arising from the mean density fluctuations, the Coriolis forces acting on the mean zonal flow, and the centripetal force due to the differential rotation arising from the largest of the advection terms. These terms combine to give

$$\nabla\langle P\rangle \approx \bar{\rho}\lambda(\Omega^2 - \Omega_0^2)\hat{\lambda} - \langle\rho\rangle g\hat{r}, \quad (15)$$

where  $\Omega = \Omega(r, \theta)$  is the angular velocity and  $\lambda = r \sin \theta$  is the distance from the rotation axis. When integrated over the domain, the relative difference between the pressure gradient and the terms on the right-hand side ( $\mathbf{R}$ ) of Equation (15), which

is given by  $\|\nabla\langle P\rangle - \mathbf{R}\|/\|\nabla\langle P\rangle\|$ , shows that this balance is satisfied to within 2% over the entire domain. The agreement is best at higher latitudes but is significant everywhere. The Coriolis and the advection terms compose about 66% of the magnitude of the gradient, while the buoyancy terms make up about 34%. Thus, the structure of the pressure arises primarily from the geostrophy of the flow (Pedlosky 1982), which is particularly important for the low-latitude peak in the pressure and temperature in the upper reaches of the convection zone. The buoyancy arising from the mean density fluctuations, however, is also important. This term follows from the equation of state (Equation (8)) and arises from the baroclinicity of the flow. Indeed, the differential rotation plays a crucial role in determining the structure of these fields.

## 6.2. Thermal Signature of Differential Rotation

If the planetary vorticity of a system is large relative to the turbulent vorticity, the Rossby number is small, which is the case in the simulations conducted in this paper (see Table 2). In these systems, the dynamics that arise tend to minimize variations across cylinders aligned with the rotation axis. Indeed, in constant density settings, the Taylor–Proudman theorem states that there is no variation along these cylinders. On the other hand, the density and pressure isosurfaces can lose alignment in stratified flows, leading to baroclinicity and flows that can violate this constraint as is seen in the cylinder crossing meridional circulation in Figures 3 and 4. One might suspect that given the large equator-to-pole thermal contrast established in these simulations, a strong meridional circulation would arise to wipe it out. As will be shown in the following section (Section 7), the differential rotation and turbulent Reynolds stresses mediate the mean meridional flow; thus, another mechanism must act to maintain this large thermal contrast. In the simulations reported on here, there is a balance between latitudinal enthalpy flux and entropy diffusion that establishes the thermal contrast, which in turn evolves in conjunction with the meridional flow and differential rotation. It is clear from the previous section that quasi-geostrophic flow accounts for a portion of the average temperature fluctuations, where the differential rotation leads to temperature perturbations, while another mechanism is responsible for the ageostrophic component.

The bulk rotation of these simulations is sufficiently rapid to increase the axial alignment of the convective structures, which leads to a more cylindrically aligned transport of enthalpy and angular momentum. The domains are highly stratified, and thus baroclinicity plays an important role in them. These tendencies lead to a mean thermodynamic state and the two mean flows (the meridional circulation and the differential rotation) that are closely coupled and maintained through the time-averaged properties of the turbulent transport of energy and momentum. We here explore the connection between the mean thermal structures and the differential rotation by examining the zonal vorticity equation, which is the azimuthal component of the curl of the momentum equation divided by the background density as detailed in Brun et al. (2011). We begin with the time-averaged and azimuthally averaged zonal vorticity equation that has been divided by  $\Omega_0^2$  in order to aid our assessment of how the various terms scale with rotation rate. It is important to note that the advection terms can be split into three contributing pieces, those due to the mean zonal velocity, the mean meridional circulation, and the Reynolds stresses arising from the fluctuating velocities. The advection term arising from the mean zonal velocity cancels the contribution from the Coriolis force, leaving the quadratic

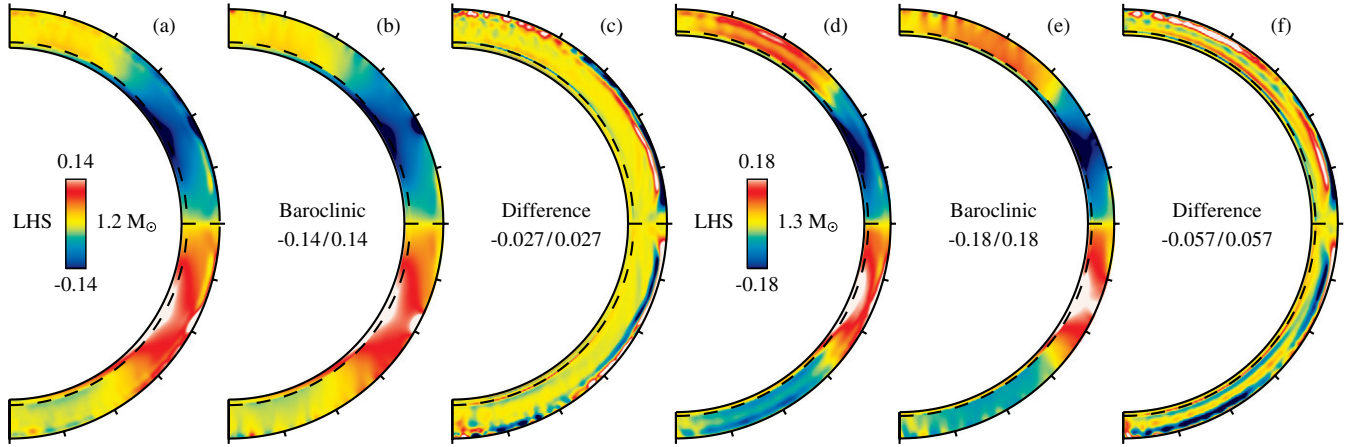


**Figure 10.** Components of the time-averaged and azimuthally averaged zonal vorticity balance. (a) Depicts the left-hand side of Equation (16), (b) the baroclinic terms, and (c) their difference, which is composed of the viscous and Reynolds stresses, for *Case A10*. (d)–(f) Show the same quantities for *Case B10*. The color tables used in each panel are scaled by the indicated values.

(A color version of this figure is available in the online journal.)

dependence on the angular velocity seen on the left-hand side of the following equation:

$$\frac{\overbrace{\lambda \frac{\partial \Omega^2}{\partial z}}^{\text{RODR}}}{\Omega_0^2} = \frac{\overbrace{\frac{g}{\Omega_0^2 r C_P} \frac{\partial \langle S \rangle}{\partial \theta} + \frac{1}{\Omega_0^2 r \bar{\rho} C_P} \frac{\partial \bar{S}}{\partial r} \frac{\partial \langle P \rangle}{\partial \theta}}^{\text{Baroclinicity}}}{\underbrace{\frac{1}{\Omega_0^2} \langle \text{RS} \rangle}_{\text{Ro}^2} + \underbrace{\frac{1}{\Omega_0^2} \langle \text{MC} \rangle}_{\text{Ro}_{\text{mc}}^2} + \underbrace{\frac{1}{\Omega_0^2} \langle \text{VS} \rangle}_{\text{Ek Ro}}}, \quad (16)$$

where  $z = r \cos \theta$  is the axial coordinate and the overbraces and underbraces indicate the scaling of a particular term with its associated Rossby number (Ro) and label the baroclinic terms. The baroclinic terms have been simplified using Equation (3). The viscous stresses  $\langle \text{VS} \rangle$  scale as the Ekman number ( $\text{Ek} = \text{Ta}^{-1/2}$ ) times the Rossby number. The turbulent Reynolds stresses  $\langle \text{RS} \rangle$  arising from the fluctuating velocity component subsequently are proportional to the fluctuating Rossby number ( $\text{Ro}'$ ), and the advection of the meridional vorticity by the meridional circulation  $\langle \text{MC} \rangle$  varies with  $\text{Ro}_{\text{mc}}$ . These stresses are given explicitly by

$$\langle \text{RS} \rangle = \langle \mathbf{u}' \cdot \nabla \omega'_\phi \rangle + \left\langle \frac{u'_\phi \omega'_\lambda}{\lambda} \right\rangle - \langle \omega' \cdot \nabla u'_\phi \rangle - \left\langle \frac{u'_\lambda \omega'_\phi}{\lambda} \right\rangle - \left\langle \omega'_\phi u'_r \frac{\partial \ln \bar{\rho}}{\partial r} \right\rangle, \quad (17)$$

$$\langle \text{MC} \rangle = \langle \mathbf{u}_{\text{mc}} \cdot \nabla \langle \omega_\phi \rangle - \frac{\langle \omega_\phi \rangle \langle u_\lambda \rangle}{\lambda} - \langle \omega_\phi \rangle \langle u_r \rangle \frac{\partial \ln \bar{\rho}}{\partial r}, \quad (18)$$

$$\langle \text{VS} \rangle = \frac{1}{\bar{\rho} r} \left\langle \frac{\partial}{\partial \theta} \nabla \cdot \mathcal{D} \cdot \hat{\mathbf{r}} \right\rangle - \left[ \frac{1}{r} - \frac{\partial \ln \bar{\rho}}{\partial r} + \frac{\partial}{\partial r} \right] \langle \nabla \cdot \mathcal{D} \cdot \hat{\boldsymbol{\theta}} \rangle. \quad (19)$$

Here,  $\lambda$  is the cylindrical radius and  $\omega_\lambda$  and  $u_\lambda$  are the cylindrically radial directed vorticity and velocity, respectively. Within the convection zone of these simulations, the pressure contribution to the baroclinic terms is small, but it becomes appreciable in the stable region and is retained. The Reynolds stresses of the fluctuating velocities ( $\mathbf{u}'$ ) in Equation (17) possess two primary components of stretching and advection. The first two terms of this equation are the advection of the zonal vorticity

and the second two are the vortical stretching of the zonal velocity, and the last term arises from the compressibility of the flows. The terms associated with the meridional circulation ( $\mathbf{u}_{\text{mc}}$ , Equation (18)) are similar in that the meridional flow advects meridional vorticity and retains the effects of compressibility, but they lack vortical stretching with contributions from only the component due to the geometry ( $\langle \omega_\phi \rangle \langle u_\lambda \rangle / \lambda$ ). The definition of  $\mathcal{D}$  from Equation (5) is used here for the viscous stress terms given in Equation (19).

Consistent with the strong thermal gradients seen in Table 3 and discussed in Section 6, Figure 10 demonstrates the extent to which the baroclinic terms are linked to the differential rotation through a meridional force balance. Indeed, from Equation (16) it is clear that the cylindrical gradient of the square of the angular velocity (labeled LHS in Figures 10(a) for case *Case A10* and 10(d) for *Case B10*) is almost entirely balanced by the latitudinal gradients of the entropy and pressure. These two thermal gradients arise due to the baroclinicity of the flows and are labeled as such in Figures 10(b) and (e). The entropy gradient dominates the meridional force balance within the convection zone because the pressure gradient is weighted by the nearly adiabatic mean entropy gradient. Within the stable region, however, the mean entropy gradient is about four orders of magnitude larger than in the convection zone, leading to a significant contribution from the latitudinal gradient of the pressure. The baroclinic terms in the bulk of the convection zone change sign at higher latitudes. This reversal in sign occurs at a lower latitude in the  $1.3 M_\odot$  cases, at about  $\pm 45^\circ$  rather than  $\pm 60^\circ$  as in the  $1.2 M_\odot$  cases. The presence of the latitudinal pressure gradient causes the large negative structure that occurs around the tangent cylinder in the northern hemisphere (positive in the south) to stretch to the poles in the stable region.

The balance, however, is not perfect as there are effects near the upper boundary that are primarily due to the Reynolds stresses associated with the turbulent velocity field, as has been seen in previous simulations of G-type stars (e.g., Brun et al. 2011; Brown et al. 2008; Brun & Toomre 2002). These departures from a pure thermal wind balance are easily seen in Figures 10(c) and (f), where the difference between the angular velocity gradient and the baroclinic terms is shown for *Case A10* and *Case B10*. It is also apparent that the turbulent Reynolds stresses play more of a role in the  $1.3 M_\odot$  simulations than in those of the  $1.2 M_\odot$  F-type stars, where the rms values of

the Reynolds stresses contribute to about 10% of the balance versus 5% for the lower mass  $1.2 M_{\odot}$  F-type stars. This is expected given that the fluctuating Rossby number in *Case B10* is larger than in *Case A10* as seen in Table 2. There are additional contributions from the viscous stresses and the advection terms associated with the meridional circulation, but they play a much smaller role in the meridional force balance than the baroclinicity and turbulent Reynolds stresses. Indeed, the importance of these various terms scales well with the values of the Rossby numbers given in Table 2, with the viscous stresses being proportional to  $\text{Ek Ro} \approx 10^{-4}$  and  $\langle \text{MC} \rangle$  varying as  $\text{Ro}_{\text{mc}}^2 \approx 10^{-4}$ . For comparison,  $\langle \text{RS} \rangle$  scales as  $\text{Ro}^2 \approx 10^{-1}$ . Accordingly, we may safely neglect these small contributions to the meridional force balance due to  $\langle \text{MC} \rangle$  and  $\langle \text{VS} \rangle$ . This leads to an expected proportionality of the baroclinic terms in Equation (16) of  $\text{Ro}_{\text{DR}} + \mathcal{O}(\text{Ro}^2) \approx \text{Ro}$ .

## 7. MAINTAINING MEAN FLOWS

The convective motions in these simulations are influenced by the bulk rotation, spherical geometry, and stratification of the domain. The mean flows and thermodynamic structures, such as those described above, are established and maintained by the transport of momentum and energy supported by these motions. Here we will consider how the transport of angular momentum leads to a co-evolution of and a direct link between the meridional circulation and the differential rotation. To illustrate the subtle balances achieved within this turbulent convection that lead to the maintenance of these mean flows, consider the time-averaged and azimuthally averaged zonal component of the momentum equation (Miesch & Hindman 2011), which yields the evolution equation for the specific angular momentum

$$\langle \rho \mathbf{u} \rangle \cdot \nabla \mathcal{L} = -\nabla \cdot \left[ F_{\lambda} \hat{\lambda} + F_z \hat{z} \right] \equiv \mathcal{T}, \quad (20)$$

$$F_{\lambda} = \bar{\rho} \lambda \langle u'_{\lambda} u'_{\phi} \rangle - \bar{\rho} v \lambda^2 \frac{\partial \Omega}{\partial \lambda}, \quad (21)$$

$$F_z = \bar{\rho} \lambda \langle u'_z u'_{\phi} \rangle - \bar{\rho} v \lambda^2 \frac{\partial \Omega}{\partial z}, \quad (22)$$

where  $\mathcal{L} = \lambda^2 \Omega = \lambda (\langle u_{\phi} \rangle + \lambda \Omega_0)$ ,  $\lambda = r \sin \theta$  is the cylindrical radius,  $\mathbf{u}' = \mathbf{u} - \langle \mathbf{u} \rangle$  is the fluctuating velocity,  $\hat{\lambda}$  is the cylindrical radial unit vector, and  $\langle \mathbf{u} \rangle$  is the axisymmetric velocity. The advection of angular momentum by the meridional flow could be incorporated into the flux but is retained separately for later analysis. The axial torque  $\mathcal{T}$  is the divergence of the sum of both the radial and cylindrical angular momentum fluxes, which are due to the viscous stresses arising from the mean zonal velocity and the Reynolds stresses produced by the turbulent alignment of the cylindrical and radial velocity components with the fluctuating longitudinal component. These transport mechanisms act in concert during the evolution of a case to accelerate the equator and decelerate the poles until a steady state is reached in which the axial torques act to balance the meridional advection of angular momentum, while also helping to maintain the differential rotation. The axial torque for *Case A10*, as well as the angular momentum fluxes that contribute to it, is shown in Figure 11.

In a statistically steady state where  $\partial \mathcal{L} / \partial t \approx 0$ , the angular momentum advected by the meridional flows must balance the net torque  $\mathcal{T}$  as in Equation (20). Although the angular velocity profile  $\Omega$  of these simulations is roughly conical at

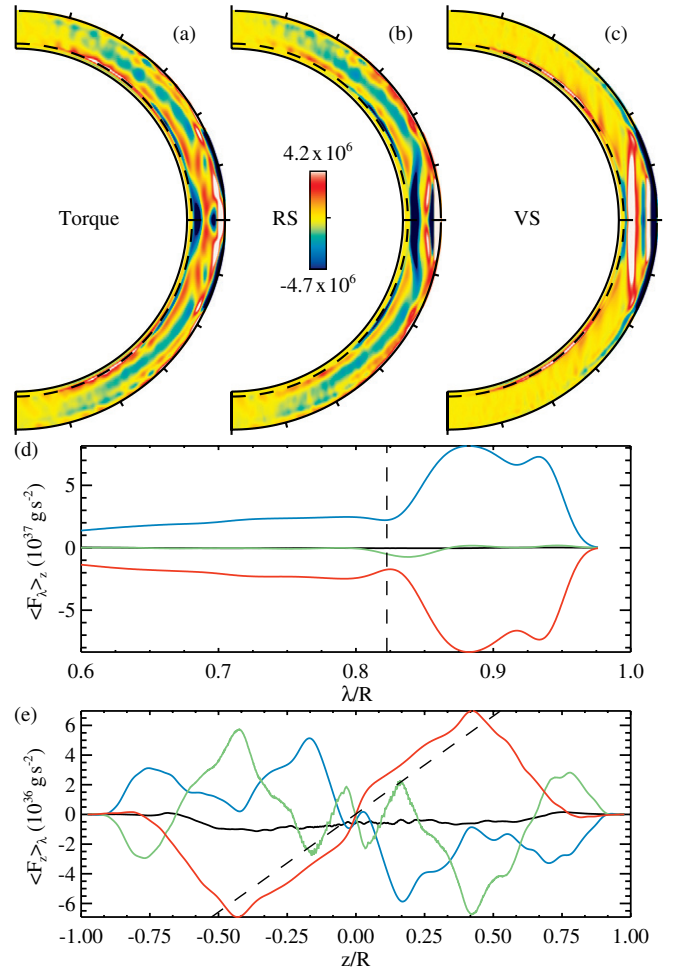


**Figure 11.** Axial torques that balance the meridional advection of angular momentum are shown for *Case A10*. (a) The net axial torque of the right-hand side of Equation (20). (b) The axial torque due to Reynolds stresses (RSs). (c) The axial torque due to viscous stresses (VSs). (a)–(c) are scaled relative to the net torque and shown in units of  $\text{g cm}^{-1} \text{s}^{-2}$ . (d) Vertically integrated angular momentum fluxes in the cylindrical radial direction ( $\langle F_{\lambda} \rangle_z$ ) and (e) cylindrical angular momentum fluxes integrated over the cylindrical radius ( $\langle F_z \rangle_{\lambda}$ ) with RSs as blue lines, transport by the meridional circulation in green, VSs in red, and the total in black. The dashed line in (d) indicates the value of  $\lambda$  at the tangent cylinder at the base of the convection zone. In (e) the dashed line shows the values of  $z$  along the tangent cylinder until it intersects the upper radial boundary.

(A color version of this figure is available in the online journal.)

most latitudes, as shown in Figures 3 and 4, the specific angular momentum  $\mathcal{L}$  is much more cylindrical, increasing away from the rotation axis due to the weighting by the square of the lever arm. For some intuition, Equation (20) can be understood by considering the largest component of the left-hand side,  $\langle \rho u_{\lambda} \rangle \partial \mathcal{L} / \partial \lambda \approx 2 \Omega_0 \lambda \langle \rho u_{\lambda} \rangle$ . This approximate relationship implies that the axial torque is balanced largely by the cylindrically radial component of the meridional flow. Moreover, this can be interpreted as  $\langle \rho u_{\lambda} \rangle \approx \mathcal{T} / 2 \Omega_0 \lambda$ , namely, that an axial torque induces a meridional flow either toward or away from the rotation axis depending on its sign. Thus, Equation (20) implies that a net prograde torque ( $\mathcal{T} > 0$ ) will induce a steady meridional flow away from the rotation axis, while a retrograde torque ( $\mathcal{T} < 0$ ) will generate a flow toward the rotation axis. Thus, the steady state meridional circulation is achieved in part through the Coriolis force acting on the mean zonal flow, a process referred to as gyroscopic pumping (e.g.,

McIntyre 1998; Wood & McIntyre 2007; Miesch & Hindman 2011).

### 7.1. Decrypting the Axial Torques

Figure 11 depicts the balance of the axial torques expressed in Equation (20) that is established in *Case A10*, averaged over approximately 30 rotation periods. The sum of the torques due to the Reynolds and viscous stresses (Figures 11(b) and (c)) balances the meridional advection of angular momentum so closely that it is visually indistinguishable from Figure 11(a), and thus the left-hand side of Equation (20) is not included in the figure. This indicates that the mean flows have indeed reached an equilibrium state, as can be deduced from the very small departure from zero of the integrated total cylindrical radial and axial angular momentum fluxes shown in Figures 11(d) and (e). The net axial torque shown in Figure 11(a) illustrates that there is a prograde equatorial torque and retrograde torque inside the tangent cylinder as one would expect given the sense of the differential rotation (see Sections 3.1 and 3.2). The mean net torque is sustained over a long period of time, as the average taken here is over several hundred rotational periods. Given that energy is conserved within the system, this implies that energy is being transferred from the thermal state to the kinetic energy of the system and through dissipation it is transferred back to the thermal reservoir.

By comparing Figures 11(a) and (b), it is apparent that the Reynolds stresses are the dominant mode of angular momentum transport inside of the tangent cylinder. In the regions above  $45^\circ$  latitude, the axial component of the Reynolds stress transports angular momentum outward along cylinders and is balanced by the meridional circulation advecting angular momentum inward, as is seen in Figures 11(a) and (e). At mid-latitudes between the tangent cylinder and about  $45^\circ$ , the radial component of the Reynolds stress angular momentum flux is positive, so angular momentum is transported toward the surface, but it then reverses sign above  $45^\circ$ . The torque resulting from the divergence of these Reynolds stress angular momentum fluxes is negative at mid-depth, decelerating the mid-convection zone, and positive at the boundaries, thus accelerating the upper convection zone and the overshooting region (Figure 11(b)). Inside the tangent cylinder, the downflow plumes are nearly aligned with the rotation axis and tend to conserve their angular momentum. This supports an inward angular momentum transport and results in the zonal deceleration seen at higher latitudes and throughout the bulk of the convection zone. However, the downflows are buoyantly braked and diverge as they approach the bottom of the convection zone and enter the overshooting region. During this process, the flows begin to dilate and become anti-cyclonic so that they accelerate the lower convection zone and overshooting region. This torque results in a gyroscopically pumped meridional flow that is equatorward near the base of the convection zone and poleward closer to the surface, where it must cross  $\mathcal{L}$  contours (Figures 3(h) and 11(b)).

Outside the tangent cylinder, where the columnar convective structures are so prominent, the viscous and the Reynolds stresses are of nearly equal importance. The integrated fluxes shown in Figures 11(d) and (e) reflect this balance. A strong columnar feature saturates the color table and is visible in the viscous and Reynolds stress torques (Figures 11(b) and (c)), where it nearly follows the tangent cylinder as is clear in Figure 11(e). The Reynolds stresses arise from the thin, spiraling, columnar equatorial convective cells. The properties of the torque due to Reynolds stresses associated with these structures

are clear; they act to reduce the angular momentum at depth and increase it nearer the surface, while the viscous stresses attempt to counteract this action but are slightly weaker. The axially aligned equatorial flows seen in these simulations are strongly affected by the boundary geometry. In Busse (2002), it is shown that the convex curvature of the caps of the cylindrical annular convective domain geometry leads to prograde tilted columnar cells. These tilted columns transport prograde momentum outward and retrograde angular momentum inward, as occurs with the equatorial convection cells here. This occurs because the thermal Rossby wave associated with the columnar convection tends to propagate faster in the upper convection zone and slower in the lower convection zone (Busse & Hood 1982). The prograde torque of the Reynolds stresses above the mid-convection zone and the retrograde torque in the lower convection zone and overshooting region, visible in Figure 11(b), indicate that these equatorial convective structures do indeed play a crucial role in the angular momentum transport. This is manifest in the radial dependence of the angular velocity (Figures 3 and 4).

There are two sets of equatorial columns in this simulation. One set of columns is confined to the deep convection zone, terminating at the base of the convection and extending up to the middle of the convection zone. A second set of columns exists at the upper boundary and extends down to the middle of the convection zone. This situation arises because the radial differential rotation is large enough to shear the columns and because the density scale height acts to confine columns near the upper boundary, which can be understood as a result of a large Taylor number. This configuration of columns manifests itself in the axial torque as a region of negative torque at the base of the convection zone, a positive torque just below the middle of the convection zone, a negative torque at the base of the outer columns, and a positive torque near the upper boundary as in Figure 11(b).

In the limit that the outer boundary becomes spherical, the equatorial columns described in Busse (2002) become increasingly sheared in longitude with increasing latitude, where the fastest prograde flows are at the equator and are slower near the latitude at which the tangent cylinder intersects the upper boundary. This process is accentuated by the thin-shell geometry of the F-type stars, where the spherical upper boundary has an increasing slope as one approaches the equator, which in turn causes the phase speed of the thermal Rossby waves to increase. This leads to faster equatorial flows and slower flows at higher latitudes. The net axial torque reflects these effects, with a retrograde torque (flux divergence) at low latitudes between the tangent cylinder and about  $\pm 8^\circ$  and a prograde torque (flux convergence) near the equator (Figure 11(a)).

### 7.2. Meridional Flows Induced by Axial Torques

The Reynolds stresses arising from the convective cells outside the tangent cylinder are not perfectly cylindrical and have a convergent structure, where the latitude of the outer boundary of the cell is dependent on the spherical radius as is evident in Figures 11(a) and (b). On the other hand, the viscous stresses in the bulk of the convection zone are nearly cylindrical. The slight misalignment of these two torques gives rise to the net torque, as they almost cancel one another outside of the tangent cylinder (Figure 11(d)). Indeed, the complicated morphology of the net torque gives rise to four reversals in the sign at the equator, resulting in four cells of low-latitude meridional flow (Figures 11(a) and 3(h)). These cells close on the equator and either end at very low latitudes or merge and stretch up to the

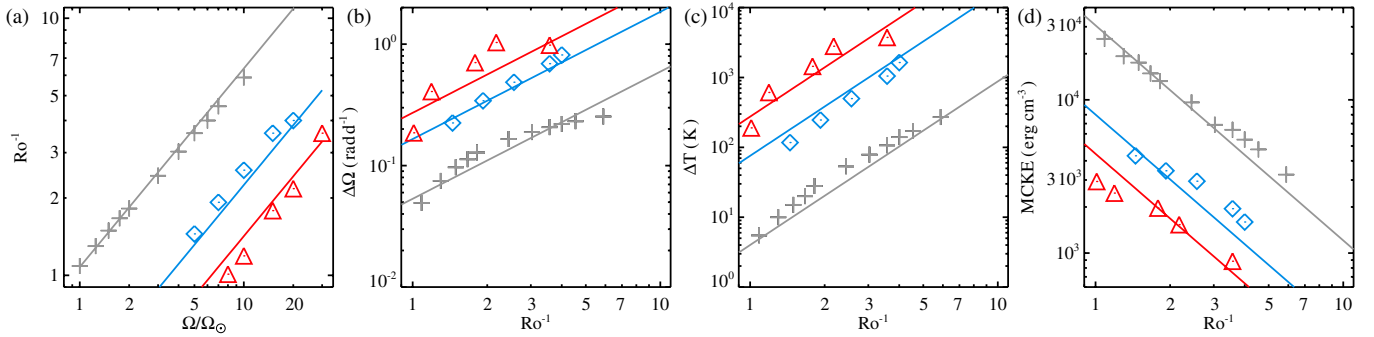


**Figure 12.** Scaling of the inverse Rossby number with mass and rotation rate, as well as latitudinal differential rotation ( $\Delta\Omega$ ), latitudinal thermal contrasts ( $\Delta T$ ), and the volume-averaged meridional circulation kinetic energy ( $\text{KE}_{\text{MC}}$ ) with mass and inverse Rossby number. (a) Inverse Rossby number for F-type star *Case A* simulations (diamonds) and *Case B* simulations (triangles), and for  $1.0 M_{\odot}$  G-type star simulations (crosses) (from Brown et al. 2008). The fit to the Rossby number is shown as solid colored lines: blue, red, and gray for the *Case A*, *Case B*, and G-type star simulations, respectively. These symbols and colored lines are employed in the following panels: (b)  $\Delta\Omega$  with the solid lines as in Equation (24); (c)  $\Delta T$  with the lines given in Equation (30); (d)  $\text{KE}_{\text{MC}}$  with lines given in Equation (37). (A color version of this figure is available in the online journal.)

tangent cylinder. At latitudes below the tangent cylinder, but above the lowest latitudes, there are two meridional cells. In the northern hemisphere, a clockwise circulation is centered on the tangent cylinder and the CCW circulation at larger cylindrical radii is a combination of a cylindrical cell at mid-convection zone and a curved cell that stretches along the outer boundary.

A similar balance of angular momentum fluxes is realized in both the *Case B* simulation at  $10 \Omega_{\odot}$  and also at other rotation rates. The trend is that there are a larger number of meridional circulation cells outside the tangent cylinder with faster bulk rotation rates, while the equatorial region remains isolated from the higher latitudes by the meridional circulation cells at the tangent cylinder. At higher latitudes inside the tangent cylinder, the Reynolds stresses support a dual-celled meridional circulation at higher rotation rates. These two cells are split in radius, one nearer the surface and one at depth. The upper cell connects with the cell that sits on the tangent cylinder, moving fluid with lower angular momentum from the upper layers at high latitudes to the base of the convection zone, which is then whisked poleward by the polar circulation cell at the base of the convection zone. However, in cases with the shear instability (Section 3.5) there is a substantial peak in both the diffusive and Reynolds stress components of the angular momentum transport at higher latitudes inside the tangent cylinder not seen in other cases. The time dependence of the instability leads to angular momentum fluxes that fluctuate much more than in the cases that do not have this instability.

## 8. SCALING WITH ROTATION AND MASS

With our choices in the scaling of the diffusivities with rotation rate, the parameter space covered by these simulations is essentially restricted to varying the rotation rate (or Rossby number) and mass of the system. Thus, we explore the variation of the differential rotation ( $\Delta\Omega$ ), meridional circulation ( $\text{KE}_{\text{MC}}$ ), and latitudinal temperature gradient ( $\Delta T$ ) with these parameters. The latitudinal differential rotation is not known a priori and is fit for; however, the latitudinal temperature gradient follows directly from  $\Delta\Omega$  given the quasi-geostrophy and thermal wind balance of the flow. The energy associated with the meridional circulation also follows from the differential rotation, but through the mechanism of gyroscopic pumping and the influence of the Reynolds stresses.

The Rossby numbers of these simulations and those in Brown et al. (2008) (see Table 2 and Figure 12(a)) are fit as a function

of mass (with  $M$  between  $1.0 M_{\odot}$  and  $1.3 M_{\odot}$ ) and bulk angular velocity ( $\Omega_0$ ), which yields

$$\text{Ro} = \frac{\langle |\omega| \rangle}{2\Omega_0} \propto M^{5.7} \Omega_0^{-0.77}. \quad (23)$$

This is close to the value expected from mixing-length theory, where  $\text{Ro}_{\text{mlt}} = v_{\text{mlt}}/R\Omega_0$  and  $v_{\text{mlt}} = (L/R^2\rho_{\text{cz}})^{1/3}$ . In the mass range of stars covered here, the depth of the convection zone decreases rapidly, so we restrict our consideration to stellar masses between  $1 M_{\odot}$  and  $1.3 M_{\odot}$ . In this range, the mean density of the convection zone scales as  $\rho_{\text{cz}} \propto M^{-15.5}$ , while the radius and luminosity of the stars simulated here are proportional to  $R \propto M$  and  $L \propto M^4$ . This implies that the mixing length velocity scales as  $v_{\text{mlt}} \propto M^{5.8}$ , which leads to an estimate of the Rossby number that scales as  $\text{Ro}_{\text{mlt}} \propto M^{4.8} \Omega_0^{-1}$ . The exponents of the mass and rotation rate for this estimate are close to the fit to the Rossby number shown above but imply a slightly smaller dependence on the mass and more dependence on the rotation rate. In laboratory experiments (Aubert et al. 2001), the Rossby number is found to scale as  $\text{Ro}_{\text{exp}} \approx (\text{Ra}_Q \text{Ek}^3)^{2/5} \propto \Omega_0^{-1.2}$ , where  $\text{Ra}_Q = \text{RaNu}$  is the heat-flux-based Rayleigh number,  $\text{Nu}$  is the Nusselt number, and  $\text{Ek}$  is the Ekman number. We find that our stellar convection simulations scale similarly to the experiments where  $\text{Ro} \propto \text{Ro}_{\text{exp}}^{1/2} = (\text{Ra}_Q \text{Ek}^3)^{1/5}$  with  $\text{Ra}_Q$  sampled at mid-domain.

Numerical simulations, on the other hand, suggest that the Rossby number is inversely proportional to a power of the rotation rate that is less than unity. This scaling is exhibited here, in G-type star simulations using ASH (Brown et al. 2008), in spherical shell segments (Käpylä et al. 2011), and in Cartesian f-plane simulations (Käpylä et al. 2004). The rotational scaling of the Rossby number in these simulations, with a power less than one, is expected given the influences of rotation on the convective patterns and the rms velocities of the flow, effects that mixing-length theory does not explicitly treat. One can see this directly from the convective flux in the simulations, where it can be greater or less than the luminosity of the star depending on the rotation rate. This leads to a mixing-length velocity that varies with rotation rate and thus a more complicated dependence of the Rossby number on the rotation rate.

On our path through parameter space, a complication arises, where there is a threshold bulk rotation rate  $\Omega_{\text{th}}$  below which the differential rotation becomes anti-solar. Such behavior is seen in both simulations of spherical domains and Cartesian domains

at various levels of turbulence in both the ASH simulations (Brun & Palacios 2009; Matt et al. 2011) and simulations carried out in Cartesian domains (Käpylä et al. 2004), as well as in spherical segments (Käpylä et al. 2011). We observe that this transition between solar-like and anti-solar-like differential rotations occurs within flows that have a Rossby number of nearly one. It is also apparent that this change in the rotational behavior of the simulations is a function of mass, as it occurs around  $0.8 \Omega_{\odot}$  for  $1.0 M_{\odot}$  G-stars in Brown et al. (2008), near  $4 \Omega_{\odot}$  for the  $1.2 M_{\odot}$  F-type stars, and at about  $7 \Omega_{\odot}$  for the  $1.3 M_{\odot}$  F-type stars. We have been working to understand how and why there is this branch of solutions possessing anti-solar-like differential rotation, and we will be subsequently reporting on it with models of F-, G-, and K-type stars. Briefly, this transition arises from overdriven convection occurring due to our choices of boundary conditions, diffusion profiles, and initial stratification, all of which result in a Rossby number greater than one throughout the bulk of the convection zone and a reversal in the sign of the Reynolds stresses for rotation rates below the threshold. However, due to the existence of this branch of solutions, we have chosen the bulk rotation rates of the simulations reported on here to be above this threshold rotation rate.

### 8.1. Differential Rotation

The relative latitudinal differential rotation ( $\Delta\Omega/\Omega_0$ ) established in these simulations is measured between the equator and  $60^\circ$  latitude (Table 3). The relative radial differential rotation measured between the bottom of the domain and the top at the equator is also shown in Table 3. The trend for increasing relative latitudinal differential rotation at lower rotation rates and decreasing  $\Delta\Omega/\Omega_0$  at higher rotation rates is clear. There is a peak in  $\Delta\Omega/\Omega_0$  in both the  $1.2 M_{\odot}$  and  $1.3 M_{\odot}$  simulations, with the former achieving a maximum around  $7 \Omega_{\odot}$  and the latter at  $20 \Omega_{\odot}$ . In Brown et al. (2008), a peak in the latitudinal differential rotation is reached at about  $2 \Omega_{\odot}$ . These maxima, however, are sensitive to the level of turbulence in both the simulations as shown in Brown et al. (2008), which is likely also the case here but is not explicitly explored.

An intriguing feature of these simulations is that the absolute differential rotation in both radius and latitude increases with rotation rate (decreasing Rossby number), as seen in Figure 12. It is also apparent that the mass of the star plays an important role through its influence on the depth of the convection zone, as well as the strength of the convective driving arising from the increased luminosity of the star. Indeed, we find here that the absolute latitudinal differential rotation  $\Delta\Omega_{60}$  established in these simulations, and measured between the equator and  $60^\circ$  latitude, scales with the mass of the star and the inverse of the Rossby number as

$$\Delta\Omega_{60} = 8.3 \times 10^{-2} \text{ rad day}^{-1} \left(\frac{M}{M_{\odot}}\right)^{3.9} \left(\frac{\Omega_0}{\Omega_{\odot}}\right)^{0.6} \quad (24)$$

$$= 5.3 \times 10^{-2} \text{ rad day}^{-1} \left(\frac{M}{M_{\odot}}\right)^{6.2} \text{Ro}^{-1.05}. \quad (25)$$

This scaling of the absolute latitudinal differential rotation with Rossby number and mass is shown in Figure 12(b). Although the differential rotation decreases consistently with increasing Rossby number among all the cases studied here, there is some indication from the levels of differential rotation

achieved in Brown et al. (2008) that there may be a change in the rate of increase of the absolute differential rotation at larger rates of rotation. This may arise because there is either a maximum in absolute differential rotation or simply slower growth at larger rotation rates. However, probing these higher rotation rates is beyond the current capabilities of ASH due to the exclusion of centrifugal forces.

Mass also plays a crucial role in building increasingly strong differential rotation in higher mass stars. The strong mass dependence of the fit in Equation (24) reflects the more vigorous convection and consequently larger Reynolds stresses that arise during the transition from the Sun to the slightly more massive F-type stars. The dependence of the magnitude of the differential rotation on the mass, or more concretely the dependence on effective temperature, is also clear in observations over a large range of temperatures (Barnes et al. 2005; Reiners 2006; Collier Cameron 2007). The scaling of the latitudinal differential rotation in Collier Cameron (2007) is  $\Delta\Omega \propto T_{\text{eff}}^{8.6} \propto M^{4.3}$ , where  $T_{\text{eff}} \propto M^{1/2}$ . As is evident in Equation (25), our scaling of the differential rotation is close to this observational mass scaling, within the bounds of the uncertainty of the observational data. The reason for the discrepancy in the expected mass scaling between Equations (24) and (25) is that the above fit is applied to shifted data, making the mapping between rotation rate and Rossby number more complicated. This is due to the fact that the rotation rate mass fit to the differential rotation of our models crosses zero and becomes negative below a particular value of the rotation rate that depends on the mass of the star. We remove this variation by shifting the data so that they may be fit consistently as in Equation (25).

### 8.2. Latitudinal Temperature Gradient

A striking property of the meridional force balance in Equation (16) is that increasing  $\Omega_0$  leads to increasingly cylindrical rotation profiles, as one would expect from gyroscopic pumping (Section 7). In the absence of baroclinicity, gyroscopic pumping will produce a meridional circulation that acts to make the contours of the angular momentum, and thereby the angular velocity, more cylindrical (Miesch & Hindman 2011). We find, however, that the baroclinicity of the flows increases with more rapid rotation. The scaling of the latitudinal gradients in temperature and entropy increases at a rate that nearly keeps pace with the quadratic scaling of the rotation rate, reducing the tendency for increased alignment with the rotation axis. This variation of the temperature with mass and Rossby number is shown in Figure 12(b), where  $\Delta T_{60}$  decreases substantially with increasing Rossby number (increase with increasing rotation rate) as

$$\Delta T_{60} = 5.3 \text{ K} \left(\frac{M}{M_{\odot}}\right)^{6.4} \left(\frac{\Omega_0}{\Omega_{\odot}}\right)^{1.6}, \quad (26)$$

$$= 5.3 \text{ K} \left(\frac{M}{M_{\odot}}\right)^{16.1} \text{Ro}^{-2.3}. \quad (27)$$

To understand the origin of these scalings, consider the latitudinal gradients of the entropy and pressure that scale with the ageostrophic component of the angular velocity, which in turn scales as the Rossby number. To find how the latitudinal gradient of the temperature should vary with rotation rate, we combine the geostrophic pressure balance (Equation (15)) and

the ageostrophic thermal wind (Equation (16)), which leads to the following:

$$\frac{\partial \langle T \rangle}{\partial \theta} = \frac{r \lambda \bar{T}^2}{g} \frac{\partial}{\partial z} \left[ \frac{\Omega^2 - \Omega_0^2}{\bar{T}} \right]. \quad (28)$$

This allows a simple homology relationship to be developed with the assumptions that the effective temperature and the radius of the star depend on only the mass of the star as mentioned above. We find that when integrated over latitude the temperature gradient becomes

$$\Delta T_{60} \approx \Delta T_0 \left( \frac{M}{M_\odot} \right)^{2.5} \left( \frac{\Omega_0}{\Omega_\odot} \right) \Delta \Omega \quad (29)$$

$$= \Delta T_0 \left( \frac{M}{M_\odot} \right)^{9.6} \text{Ro}^{-1.3} \Delta \Omega. \quad (30)$$

The solid curves in Figure 12(b) depict this homology relationship, where it overlays the actual values of the temperature contrast in the simulations.

### 8.3. Meridional Circulation Kinetic Energy

Volume-averaged energy densities for our simulations are shown in Table 3. At the lowest rotation rate, fluctuating convective kinetic energy (defined as  $0.5 \bar{\rho} \langle u^2 \rangle$ ,  $\text{KE}_C$ ) and the kinetic energy in the average differential rotation ( $0.5 \bar{\rho} \langle u_\phi \rangle$ ,  $\text{KE}_{\text{DR}}$ ) are comparable. As the rotation rate is increased, the  $\text{KE}_{\text{DR}}$  grows strongly and the convective energy decreases slightly, leading the  $\text{KE}_{\text{DR}}$  to dominate the total kinetic energy. The energy in meridional circulations ( $0.5 \bar{\rho} (\langle v_r \rangle + \langle v_\theta \rangle)$ ,  $\text{KE}_{\text{MC}}$ ) is always small and decreases in both magnitude and percentage of the total energy with more rapid rotation.

The volume-averaged meridional circulation kinetic energy clearly decreases with rotation rate in both these simulations and those of Brown et al. (2008). If we fit for this scaling, as we have for the absolute differential rotation, we find that

$$\text{KE}_{\text{MC}} = 2.4 \times 10^4 \text{ erg cm}^{-3} \left( \frac{M}{M_\odot} \right)^{-1.2} \left( \frac{\Omega_0}{\Omega_\odot} \right)^{-0.8} \quad (31)$$

$$= 2.4 \times 10^4 \text{ erg cm}^{-3} \left( \frac{M}{M_\odot} \right)^{-7.4} \text{Ro}^{1.04}. \quad (32)$$

We can understand this scaling by returning to the equations of gyroscopic pumping and considering the scaling of the axial torques. First, though, it is useful to extract the dependence of the stream function on the gradients of the angular momentum and the torques. Since the mean poloidal mass flux is divergenceless, the meridional flow can be represented as a stream function  $\psi$  such that  $\langle \rho \mathbf{u} \rangle = \nabla \times \psi \hat{\phi}$ . Expressing Equation (20) in terms of this stream function and then integrating the result clockwise from the lower boundary along  $\mathcal{L}$  contours, we arrive at

$$\psi = \frac{1}{\lambda} \int_C \frac{\lambda \mathcal{F}}{|\nabla \mathcal{L}|} ds, \quad (33)$$

where  $C$  is the contour of integration. The denominator in this equation is dominated by the  $\lambda$  component such that

$\nabla \mathcal{L} \approx 2 \Omega_0 \lambda$ . This reduces Equation (33) to the following:

$$\psi \approx \frac{1}{2 \lambda \Omega_0} \int_C \mathcal{F} ds \propto M^{-7.4} \text{Ro}^{1.3} \mathcal{F} [M, \text{Ro}]. \quad (34)$$

The meridional circulation kinetic energy is consequently proportional to

$$\text{KE}_{\text{MC}} = \frac{1}{V} \int_V \frac{(\nabla \times \psi \hat{\phi})^2}{\rho} dV \propto M^{-1.3} \text{Ro}^{2.6} \mathcal{F} [M, \text{Ro}]^2. \quad (35)$$

The proportionality of the torque  $\mathcal{F}$  is difficult to predict a priori. One could assume that the Reynolds stresses follow the  $\Lambda$  effect (Rüdiger 1989), in which case the axial torque associated with the Reynolds stresses in our parameter regime should scale as  $\rho_{\text{cz}} v_{\text{mlt}}^2 \text{Ro}_{\text{mlt}}^{-1} \propto M^{-4} \text{Ro}_{\text{mlt}}^{-1} \propto M^{9.8} \Omega_0$ . However, this would lead to a  $\text{KE}_{\text{MC}}$  that is constant with the rotation rate, which is clearly not the case here. Thus, without guidance to predict the scaling of the torque, it must be fit for. Indeed, we find that the Reynolds stress axial torque scales as

$$\mathcal{F} \propto M^{-3} \text{Ro}^{-0.6}. \quad (36)$$

Therefore, the  $\text{KE}_{\text{MC}}$  that arises from gyroscopic pumping (Equation (20)) is proportional to

$$\text{KE}_{\text{MC}} \propto M^{-7.3} \text{Ro}^{1.4}, \quad (37)$$

which correlates well with the  $\text{KE}_{\text{MC}}$  found in our simulations as seen in Figure 12(d) and Equation (32). That is, the torque associated with the Reynolds stresses increases with rotation rate, rather than decreases as expected from mean-field theory.

## 9. CONCLUSIONS

As is apparent from the observation of F-type stars, they rotate on average much more rapidly than does the present Sun. In these stars, rotation must strongly influence the convective motions and lead to differential rotation. Such differential rotation has been observed in many F-type stars (e.g., Reiners 2007). To assess how this differential rotation may arise, we have explored here the effects of rotation rate, convective overshooting, and stellar mass on the patterns and mean properties of the global-scale convection in simulations of two F-type stars.

We have found that the mean zonal flows of differential rotation become much stronger with more rapid rotation and larger mass, scaling as  $\Delta \Omega \propto M^{3.9} \Omega_0^{0.6}$  or as  $\Delta \Omega / \Omega_0 \propto M^{3.9} \Omega_0^{-0.4}$  (Section 8). This corresponds well with observational detections of differential rotation for increasing rotation rate (Reiners 2007) and with mass (Barnes et al. 2005; Reiners 2006; Collier Cameron 2007). Accompanying the growing differential rotation is a significant latitudinal temperature contrast, with amplitudes of 1000 K or higher in the most rapidly rotating cases. This contrast in turn scales with mass and rotation rate as  $\Delta T \propto M^{6.4} \Omega_0^{1.6}$ . The maximum temperature contrast near the surface occurs between the hot poles and the cool mid-latitudes at about  $\pm 30^\circ$ , near the tangent cylinder. These temperature fluctuations about the spherically symmetric mean temperature are decomposed into its geostrophic and ageostrophic components, both of which are linked to the rotation of the star and its baroclinicity (Section 6). If this latitudinal temperature contrast prints through the vigorous convection at the stellar surface, it may appear as an observable latitudinal variation in intensity. The thermal contrast would presumably persist for long periods

compared to stellar activity, offering a way to disentangle this intensity signature from that caused by spots of magnetism at the stellar poles.

Additionally, we have seen that the mean meridional circulation becomes much weaker with more rapid rotation and with higher mass, consistent with the concept of gyroscopic pumping, where the energy contained in these circulations drops approximately as  $KE_{MC} \propto M^{-1.2}\Omega_0^{-0.8}$ . However, the scaling of these quantities is sensitive to the variation of the Reynolds stresses, and thus their variation with the level of turbulence in the simulations must be better understood. As suggested in Brown et al. (2008, 2010), the weaker meridional circulations in more rapidly rotating stars will have a strong impact on many theories of stellar dynamo action, including the Babcock–Leighton flux–transport model favored for Sun-like stars as recently investigated (Jouve & Brun 2007; Jouve et al. 2010; Miesch & Brown 2012). Indeed, the lack of large single cells of meridional circulation at all latitudes in many models of more rapidly rotating stars suggests that the most common profile used for these flows may be oversimplified and is actually associated with anti-solar-like differential rotation.

The simulations here include a portion of the stably stratified radiative interior below the convection zone. It has been shown here and in previous works to have a significant impact on the morphology of the mean flows and on the magnitude of the latitudinal thermal contrast. The largest impact is on the thermal field, where it leads to about a 50% greater latitudinal temperature contrast but only about 10% more differential rotation. However, its inclusion does lead to a tilting of the angular velocity contours to be more conical than cylindrical, as occurs in cases without a stable region. The convection exhibited in the simulations with a stable zone yields a region of overshooting that is very slightly prolate and occupies about 1% of the star by radius.

Three of the cases presented here have exhibited a global-scale shear instability that operates within the stable region and persists for the duration of our simulations. This instability is sensitive to the magnitude and the latitudinal profile of the differential rotation and is present in both mass stars but only at higher rotation rates. It has a significant impact on the convection, causing greater depths of overshooting (Section 5), and prints through into the convection zone (Section 3.5). The instability and angular momentum transport and mixing properties associated with it will be examined in a subsequent paper (K. C. Augustson et al. 2012, in preparation).

Our simulations are hydrodynamic, and it is possible that the inclusion of magnetism may alter the scalings of differential rotation and latitudinal temperature contrast with rotation rate. Prior MHD simulations of stellar convection have demonstrated that in some parameter regimes, strong dynamo-generated magnetic fields can react back on the differential rotation, acting to lessen angular velocity contrasts as energy is transferred into the magnetic fields (e.g., Brun et al. 2005; Browning 2008). We are currently pursuing magnetic F-type star simulations, but it is still too early to say whether the scaling trends identified here for differential rotation and latitudinal temperature contrasts as a function of  $\Omega_0$  will survive. Given previous experience with G-type stars, it is likely that the general functional dependence with rotation rate is retained (Brown et al. 2010; Brown 2011). Our simulations stop short of the turbulent stellar surface, and it is thus difficult to estimate how all of the properties of the convection seen here may affect stellar observations in detail. However, we have found that the strong differential rotation

and large thermal contrasts are a robust feature over a range of parameters, and it is likely that they will have observable consequences.

The authors thank R. A. Hock, N. A. Featherstone, R. Trampedach, N. J. Nelson, B. W. Hindman, B. J. Greer, and C. Chronopolous for thoughtful discussion and helpful comments. This research is primarily supported by NASA through the Heliophysics Theory Program grants NNX08AI57G and NNX11AJ36G, with additional support for Augustson through the NASA NESSF program by award NNX10AM74H. Brown is supported in part by NSF Astronomy and Astrophysics Postdoctoral Fellowship AST 09-02004. CMSO is supported by NSF grant PHY 08-21899. Brun acknowledges financial support by the ERC through grant 207430 STARS2 and by CNRS/INSU via Programmes Nationaux Soleil-Terre and Physique Stellaire. Brun is also grateful to the University of Colorado and JILA for their hospitality. The computations were primarily carried out on Pleiades at NASA Ames with SMD grant g26133 and also utilized XSEDE resources for analysis.

## REFERENCES

- Aubert, J., Brito, D., Nataf, H. C., Cardin, P., & Masson, J. P. 2001, *Phys. Earth Planet. Inter.*, **128**, 51
- Barnes, J. R., Cameron, A. C., Donati, J.-F., et al. 2005, *MNRAS*, **357**, L1
- Bessolaz, N., & Brun, A. S. 2011, *Astron. Nachr.*, **332**, 1045
- Bouvier, J., Forestini, M., & Allain, S. 1997, *A&A*, **326**, 1023
- Brown, B. P. 2011, arXiv:1106.6075
- Brown, B. P., Browning, M. K., Brun, A. S., Miesch, M. S., & Toomre, J. 2008, *ApJ*, **689**, 1354
- Brown, B. P., Browning, M. K., Brun, A. S., Miesch, M. S., & Toomre, J. 2010, *ApJ*, **711**, 424
- Browning, M. K. 2008, *ApJ*, **676**, 1262
- Browning, M. K., Miesch, M. S., Brun, A. S., & Toomre, J. 2006, *ApJ*, **648**, L157
- Brummell, N. H., Clune, T. L., & Toomre, J. 2002, *ApJ*, **570**, 825
- Brun, A. S., Browning, M. K., & Toomre, J. 2005, *ApJ*, **629**, 461
- Brun, A. S., Miesch, M. S., & Toomre, J. 2011, *ApJ*, **742**, 79
- Brun, A. S., & Palacios, A. 2009, *ApJ*, **702**, 1078
- Brun, A. S., & Toomre, J. 2002, *ApJ*, **570**, 865
- Busse, F. H. 2002, *Phys. Fluids*, **14**, 1301
- Busse, F. H., & Hood, L. L. 1982, *Geophys. Astrophys. Fluid Dyn.*, **21**, 59
- Chandrasekhar, S. 1961, *Hydrodynamic and Hydromagnetic Stability* (Oxford: Oxford Univ. Press)
- Clune, T. L., Elliott, J. R., Miesch, M. S., Toomre, J., & Glatzmaier, G. A. 1999, *Parallel Comput.*, **25**, 361
- Collier Cameron, A. 2007, *Astron. Nachr.*, **328**, 1030
- Collier Cameron, A., Donati, J., & Semel, M. 2002, *MNRAS*, **330**, 699
- Donati, J.-F., Semel, M., Carter, B. D., Rees, D. E., & Collier Cameron, A. 1997, *MNRAS*, **291**, 658
- Dormy, E., Soward, A. M., Jones, C. A., Jault, D., & Cardin, P. 2004, *J. Fluid Mech.*, **501**, 43
- Gilman, P. A., & Glatzmaier, G. A. 1981, *ApJS*, **45**, 335
- Glatzmaier, G. A. 1984, *J. Comput. Phys.*, **55**, 461
- Glatzmaier, G. A., & Gilman, P. A. 1981, *ApJS*, **45**, 351
- Haurwitz, B. 1940, *J. Mar. Res.*, **3**, 254
- Henry, G. W., Eaton, J. A., Hamer, J., & Hall, D. S. 1995, *ApJS*, **97**, 513
- Jones, C. A., Boronski, P., Brun, A. S., et al. 2011, *Icarus*, **216**, 120
- Jones, C. A., Kuzanyan, K. M., & Mitchell, R. H. 2009, *J. Fluid Mech.*, **634**, 291
- Jouve, L., Brown, B. P., & Brun, A. S. 2010, *A&A*, **509**, A32
- Jouve, L., & Brun, A. S. 2007, *A&A*, **474**, 239
- Käpylä, P. J., Korpi, M. J., & Tuominen, I. 2004, *A&A*, **422**, 793
- Käpylä, P. J., Mantere, M. J., Guerrero, G., Brandenburg, A., & Chatterjee, P. 2011, *A&A*, **531**, A162
- Kitchatinov, L. L. 2010, *Astron. Rep.*, **54**, 1
- Longuet-Higgins, M. S. 1964, *Proc. R. Soc. A*, **279**, 446
- Marsden, S. C., Waite, I. A., Carter, B. D., & Donati, J.-F. 2005, *MNRAS*, **359**, 711
- Matt, S. P., Do Cao, O., Brown, B. P., & Brun, A. S. 2011, *Astron. Nachr.*, **332**, 897

- McIntyre, M. E. 1998, *Prog. Theor. Phys. Suppl.*, **130**, 137
- Miesch, M. S., & Brown, B. P. 2012, *ApJ*, **746**, L26
- Miesch, M. S., Brun, A. S., DeRosa, M. L., & Toomre, J. 2008, *ApJ*, **673**, 557
- Miesch, M. S., Brun, A. S., & Toomre, J. 2006, *ApJ*, **641**, 618
- Miesch, M. S., Elliott, J. R., Toomre, J., et al. 2000, *ApJ*, **532**, 593
- Miesch, M. S., & Hindman, B. W. 2011, *ApJ*, **743**, 79
- Paxton, B., Bildsten, L., Dotter, A., et al. 2011, *ApJS*, **192**, 3
- Pedlosky, J. (ed.) 1982, *Geophysical Fluid Dynamics* (Berlin: Springer)
- Rast, M. P., Ortiz, A., & Meisner, R. W. 2008, *ApJ*, **673**, 1209
- Reiners, A. 2006, *A&A*, **446**, 267
- Reiners, A. 2007, *Astron. Nachr.*, **328**, 1034
- Reiners, A., & Schmitt, J. H. M. M. 2002, *A&A*, **384**, 155
- Reiners, A., & Schmitt, J. H. M. M. 2003, *A&A*, **398**, 647
- Rempel, M. 2004, *ApJ*, **607**, 1046
- Rempel, M. 2005, *ApJ*, **622**, 1320
- Rogers, T. M., & Glatzmaier, G. A. 2006, *ApJ*, **653**, 756
- Rüdiger, G. (ed.) 1989, *Differential Rotation and Stellar Convection. Sun and the Solar Stars* (Berlin: Akademie)
- Schou, J., Antia, H. M., Basu, S., et al. 1998, *ApJ*, **505**, 390
- Silva-Valio, A., & Lanza, A. F. 2011, *A&A*, **529**, A36
- Spiegel, E. A., & Zahn, J.-P. 1992, *A&A*, **265**, 106
- Thompson, M. J., Toomre, J., Anderson, E. R., et al. 1996, *Science*, **272**, 1300
- Trampedach, R., & Stein, R. F. 2011, *ApJ*, **731**, 78
- Verner, G. A., Elsworth, Y., Chaplin, W. J., et al. 2011, *MNRAS*, **415**, 3539
- Watson, M. 1981, *Geophys. Astrophys. Fluid Dyn.*, **16**, 285
- Wood, T. S., & McIntyre, M. E. 2007, in *AIP Conf. Ser. 948, Unsolved Problems in Stellar Physics: A Conference in Honor of Douglas Gough* (Melville, NY: AIP), 303
- Zahn, J.-P. 1991, *A&A*, **252**, 179
- Zhang, K. 1992, *J. Fluid Mech.*, **236**, 535